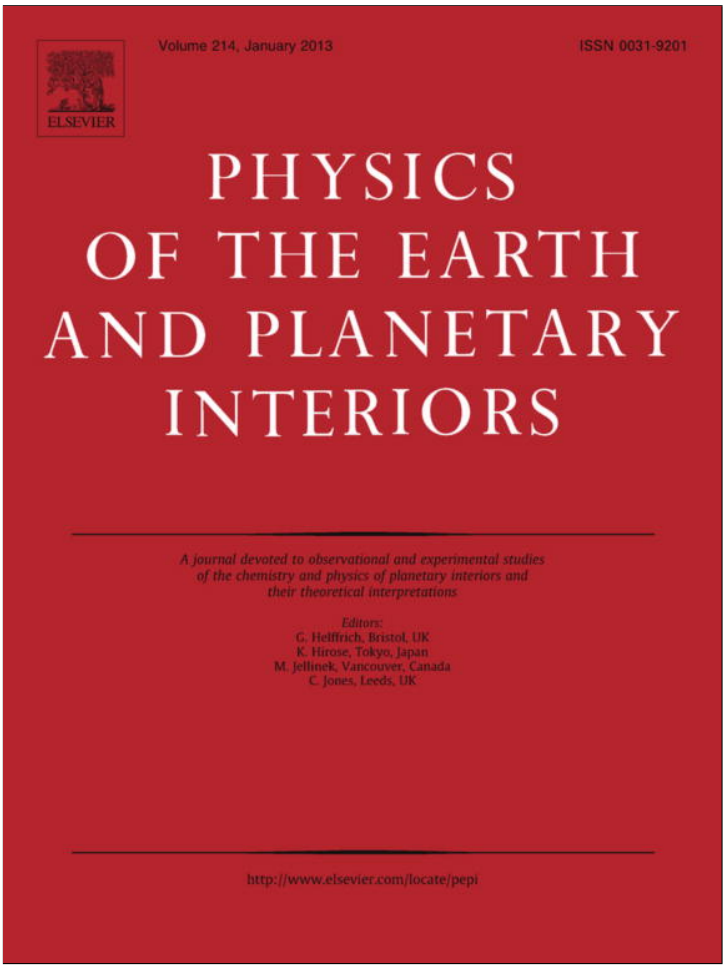

Physics of the Earth and Planetary Interiors 214 (2013) 87–103

Contents lists available at SciVerse ScienceDirect

Physics of the Earth and Planetary Interiors

journal homepage: www.elsevier.com/locate/pepi

Controls on geomagnetic reversals and core evolution by mantle convection in the Phanerozoic

Peter Olson [a,*], Renaud Deguen [a], Linda A. Hinnov [a], Shijie Zhong [b]

[a] Department of Earth and Planetary Sciences, Johns Hopkins University, Baltimore, MD 21218, USA
[b] Department of Physics, University of Colorado, Boulder, CO 80309, USA

ARTICLE INFO

Article history:
Received 25 April 2012
Received in revised form 20 September 2012
Accepted 7 October 2012
Available online 26 October 2012
Edited by Chris Jones

Keywords:
Geodynamo
Mantle convection
Polarity reversals
Pangaea
Supercontinent breakup

ABSTRACT

Numerical dynamos driven by non-uniform heat flux at the core-mantle boundary are used to investigate the connections between geomagnetic field structure, geomagnetic reversal frequency, core evolution, and mantle convection through Phanerozoic time. Polarity reversal sequences and time average magnetic field structures are calculated using dynamos driven by two representations of lower mantle history: a reconstruction of mantle convection with plate motions by Zhang and Zhong (2011) that produces time variable core-mantle boundary (CMB) heat flux and an irregular evolution of the core, and a second model based on hotspot locations with a time independent pattern of CMB heat flux derived from the present-day seismic shear wave heterogeneity of the lower mantle that produces a monotonic evolution of the core. For both mantle histories, present-day values of the dynamo control parameters are tuned to match Geomagnetic Polarity Time Scale reversal statistics for 0–5 Ma, and the time dependences of the dynamo control parameters are determined from the thermal evolution of the core, including time variability of CMB heat flow, inner core size, inner core chemical buoyancy flux, and rotation rate. The dynamo with time independent CMB heat flux shows minor fluctuations in reversal frequency with age, whereas the dynamo with time variable CMB heat flux shows reversal rate fluctuations including stable polarity at 275 and 475 Ma and frequent reversals at other times. This dynamo also produces departures from geocentric axial dipole symmetry during the time of supercontinent Pangaea and a heterogeneous growth history of the inner core.

1. Introduction

Two contrasting interpretations of the Phanerozoic history of the mantle have recently been proposed, in which the primary difference is the longevity of the lateral heterogeneity that dominates the present-day seismic structure of the lower mantle. One interpretation of lower mantle history (Burke et al., 2008; Burke, 2011) postulates that the spherical harmonic degree two structure of the present-day lower mantle heterogeneity imaged by seismic tomography has persisted for several hundred millions of years (Dziewonski et al., 2010) and perhaps longer. Supporting evidence for this interpretation comes from hotspot reconstructions (Torsvik et al., 2006) and paleomagnetic pole locations that indicate substantial true polar wander in the Mesozoic (Courtillot and Besse, 1987).

The other interpretation is based on the assumption of whole mantle convection and a more dynamic lower mantle that has evolved since the breakup of supercontinent Pangaea from a structure dominated by spherical harmonic degree one heterogeneity to its present-day, spherical harmonic degree two dominated structure (Yoshida and Santosh, 2011). Major support for this interpretation comes from reconstructions of mantle convection that include drifting continents, time-dependent plate boundaries, and evolving plate motions through the Phanerozoic (Zhang et al., 2010; Zhang and Zhong, 2011), which show this particular evolution associated with supercontinent formation and breakup. One specific prediction of the whole mantle convection-based history is that the upwelling region beneath Africa and its seismically low velocity region is a relatively young feature in comparison with the low velocity structure beneath the central Pacific. According to whole mantle convection reconstructions, the Pacific and African low seismic velocity structures predate and postdate, respectively, the breakup of Pangaea (McNamara and Zhong, 2005; Zhang et al., 2010). Another prediction is that the pattern and the magnitude of heat flux on the core-mantle boundary (CMB) have evolved. During the formation of Pangaea, according to the convection-based history of Zhang and Zhong (2011), the CMB heat flux was dominated by a spherical harmonic degree one pattern, with low heat flux where the Pacific low seismic velocity region is today and high heat flux where the African low seismic velocity region is today. With the breakup of Pangaea this

* Corresponding author.
E-mail address: olson@jhu.edu (P. Olson).

0031-9201/$ - see front matter © 2012 Elsevier B.V. All rights reserved.
http://dx.doi.org/10.1016/j.pepi.2012.10.003

CMB heat flux pattern began to change in concert with the development of the slow seismic structure beneath Africa. Specifically, the spherical harmonic degree one content of the CMB heat flux pattern diminished while its spherical harmonic degree two content increased with time. In addition to these changes in the pattern of CMB heat flux, reconstructions of mantle convection predict that the total CMB heat flow has fluctuated through the Phanerozoic in response to changes in the structure and overall speed of the convection in the lower mantle. Although these predicted fluctuations in total core heat flow are not large – convection-based mantle histories indicate they are within ±10% of the time average Phanerozoic core heat flow (Nakagawa and Tackley, 2005) – they nevertheless have the potential to affect the behavior of the geodynamo on mantle time scales.

Because the geodynamo is sensitive to conditions at the core-mantle boundary, the record of the geomagnetic field over the Phanerozoic, and in particular, the change in the frequency of geomagnetic polarity reversals, offers a test for the competing interpretations of lower mantle history described above. The sequence of geomagnetic polarity reversals in the Geomagnetic Polarity Time Scale (GPTS) is reasonably well known to 275 Ma, and although there are gaps at earlier times, a partial GPTS has been compiled for much of the Phanerozoic (Ogg, 2012). An important property of the GPTS that is relevant to the evolution of lower mantle structure is the so-called superchron cycle, in which constant polarity superchrons lasting 30–40 Myr tend to alternate with periods of frequent reversals. Specifically, the Cretaceous Superchron (123–83 Ma), the Kiaman Superchron in the Permian (310–260 Ma) and the Moyero Superchron in the Ordovician (490–460 Ma) proposed by Pavlov and Gallet (2005) alternate with periods of frequent polarity reversals at 0–20 Ma, 150–175 Ma, and 490–530 Ma, respectively, with the period 320–450 Ma being poorly resolved but known to contain reversals.

Numerical dynamos have shown that polarity reversal frequency is sensitive to the conditions near the CMB, and in particular, the magnitude and the pattern of the heat flow from the core to the mantle. Because CMB heat flow is closely related to the three dimensional structure of the lower mantle (Van der Hilst et al., 2007; Lay et al., 2008), it has long been argued that changes in lower mantle convection influence the GPTS, including the superchron cycle (Jones, 1977; Loper and McCartney, 1986; Larson and Olson, 1991; Courtillot and Olson, 2007; Petrelis et al., 2011). However, for reasons explained by Biggin et al. (2012), quantitative interpretation of the GPTS in terms of mantle dynamics involves a host of complicating factors. First, individual polarity reversals appear to be random or partly random events (Jonkers, 2007; Ryan and Sarson, 2007), and it is unclear how to properly separate the deterministic from the stochastic behavior in the GPTS (Gallet and Hulot, 1997). Second, heat flow is not the only property in the CMB region that affects the geodynamo and its reversals, and although thermal coupling is probably the best studied aspect of long term core-mantle interaction (Glatzmaier et al., 1999; Kutzner and Christensen, 2004; Olson et al., 2010), both the magnitude and the pattern of CMB heat flow are uncertain at the present-day, and even more so in the past. Lastly, the core has evolved significantly over the time period represented by the GPTS, and this evolution also affects the geomagnetic field history, including its reversals (Driscoll and Olson, 2009b). Examples of core evolution that surely influence the geodynamo include the growth of the solid inner core, the secular cooling of the core (Labrosse, 2003), changes in the strength of chemical and thermal buoyancy sources in the core over time (Aubert et al., 2009), and slowing of Earth's rotation due to tidal friction (Williams, 2000). Accordingly, the simultaneous evolution of the mantle and the core need to be considered when interpreting the long-term geomagnetic field history.

Fortunately, there is a great disparity between the characteristic time scales of overturn in the mantle (a few hundred million years) versus the fluid outer core (a few hundred years), so that on intermediate time scales (on the order of a typical magnetic polarity chron) the outer core can be considered to be in steady state in terms of its spherically averaged structure. In addition, because lateral variations of temperature and density in the outer core are negligible compared to their mantle counterparts, we assume that on these intermediate time scales the thermal action of the mantle on the core can be represented using an imposed heat flux condition on the CMB.

In this paper, we determine the response of the core and the geodynamo to the two representations of lower mantle history described above. First we calculate the thermal and chemical evolution of the core through the Phanerozoic as dictated by their respective CMB heat flow histories, including the growth of the solid inner core. Then we use numerical dynamos to calculate time average magnetic field structures and reversal sequences driven by these mantle histories, taking into account changes in outer core buoyancy, inner core size, and rotation rate. Finally, we compare our dynamo reversal sequences with GPTS reversal sequences at key times, including the three Phanerozoic superchrons and also times when the reversal rate was high.

2. Present-day heat flux on the CMB

The three dimensional structure of the present-day lower mantle as imaged by seismic tomography includes long wavelength heterogeneity that is dominated by a spherical harmonic degree two pattern (Dziewonski, 1984; Masters et al., 2000; Kustowski et al., 2008; Dziewonski et al., 2010), with seismically slow velocity beneath Africa and the central Pacific and a nearly great circle ring of seismically fast velocities that circumscribes the Pacific basin. Interpreted in terms of temperature contrasts, the high velocity circum-Pacific ring implies anomalously low temperature, thermally dense slab material sinking toward the core-mantle boundary (Ricard et al., 1993). Conversely, the low seismic velocity regions beneath Africa and the central Pacific are often interpreted as hot, dense chemical piles (McNamara and Zhong, 2005) in which small thermal plumes form around their margins (Burke et al., 2008).

The long wavelength heterogeneity in the lower mantle has significant impact on the core, producing heat flux variations on the CMB in much the same way as lithosphere age produces regular heat flux variations at Earth's surface. Based on this analogy, we expect that the heat flux is relatively high on the CMB where the lower mantle seismic velocity is high, and conversely, the CMB heat flux is relatively low where the lower mantle seismic velocity is low. Although the heat flux on the CMB is not known with great precision, seismic studies designed to infer the geothermal gradient near the base of the mantle yield (Van der Hilst et al., 2007) CMB heat flux estimates that are generally consistent with this picture. In particular, current estimates place the total CMB heat flow in the neighborhood of 10–15 TW (Lay et al., 2008) corresponding to 65–95 mW/m^2 for the average heat flux, with local variations of 20 mW/m^2 or more.

Representations of the present-day planform of CMB heat flux in numerical dynamos often assume that the lateral variations in CMB heat flux $\delta q_{\rm cmb}$ are linearly proportional to the lateral variations in seismic shear wave velocity in the lower mantle (Glatzmaier et al., 1999; Olson and Christensen, 2002; Aubert et al., 2008) for which

$$\delta q_{\rm cmb}/\bar{q}_{\rm cmb} \propto \delta V_s/\overline{V_s} \tag{1}$$

where $\overline{V_s}$ and δV_s are the spherically-symmetric and lateral variations of shear wave velocity at some depth in the lower mantle, respectively, and $\bar{q}_{\rm cmb}$ is the CMB average heat flux. Justification

for (1) is that for uniform lower mantle composition, V_s varies inversely with temperature (Trampert et al., 2004), so at those places above the CMB where V_s is larger than average, the radial thermal gradients are larger than average, and therefore the CMB heat flux is higher than average. The proportionality coefficient in (1) can be estimated from mineralogical properties of lower mantle compounds (Trampert et al., 2004), or from the results of mantle convection models. Nakagawa and Tackley (2008) and Wu et al. (2011) have shown that a simple linear relationship like (1) with a proportionality factor of about 20 is a good approximation for purely thermal mantle convection, although this relationship tends to break down where lenses of post-perovskite phase are present.

3. CMB heat flux history from mantle convection

Fig. 1 shows the average heat flux on the CMB as a function of age through most of the Phanerozoic from convection-based mantle history HF1 by Zhang and Zhong (2011). This mantle history, hereafter referred to as HF1, is driven by a combination of convection with thermal and compositional buoyancy plus surface plate motions. The surface plate motions for 0–120 Ma are from the global model of Lithgow-Bertelloni and Richards (1998). Plate motions older than 120 Ma are based on continent reconstructions in the Atlantic hemisphere by Scotese (2001) and assume fixed plate boundaries in the Pacific hemisphere. The control parameters (mantle Rayleigh number and the temperature and pressure dependence of the viscosity) have been adjusted so that the internal mantle convective velocities are comparable to the imposed surface plate velocities. The initial conditions include compositional heterogeneity in the form of a 250 km thick dense layer above the CMB. In the initial spin-up phase of the calculation, the plate configuration and plate speeds are fixed for 150 Myr to allow the mantle thermal and compositional heterogeneity to equilibrate with the flow. In the second phase, the plate configuration and speeds are varied in stages for the next 450 Myr.

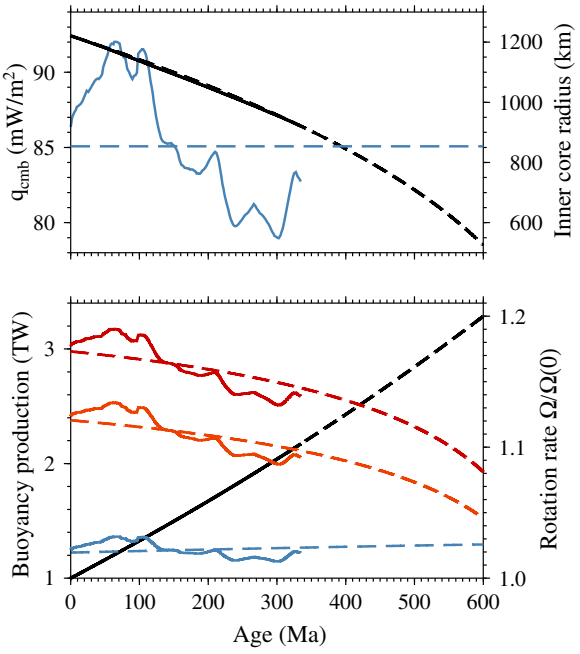

Fig. 1. Models of core evolution 0–600 Ma. Top: average CMB heat flux and inner core radius versus age; Bottom: core buoyancy production (red = total ICB, orange = compositional, blue = CMB heat flow buoyancy productions, respectively) and rotation angular velocity (relative to the present-day) versus age. Solid curves: core evolution with time variable CMB heat flow from mantle history HF1 by Zhang and Zhong (2011); Dashed curves: core evolution assuming constant CMB heat flow. (For interpretation of the references to color in this figure legend, the reader is referred to the web version of this article.)

As seen in Fig. 1, the average CMB heat flux varies between about 90 mW/m^2 at 71 Ma to 79 mW/m^2 at 300 Ma, with the present-day value 85.4 mW/m^2 being very close to the 0–475 Ma average. The decrease in average CMB heat flux prior to 300 Ma is a consequence of the assembly of Pangaea, when the average plate velocity dropped by nearly 40% in the Scotese (2001) reconstruction. Conversely, the increase in average CMB heat flux starting around 120 Ma corresponds to a 30% spike in plate speed during the Cretaceous in the Lithgow-Bertelloni and Richards (1998) plate tectonic reconstruction. In addition to temporal changes in the average CMB heat flux, there are temporal changes in the pattern and the amplitude of CMB heat flux heterogeneity in the Zhang and Zhong (2011) mantle history, including a transition from high to low heat flux beneath the present-day location of Africa associated with the switch from a pattern dominated by spherical harmonic degree one during Pangaea to a pattern dominated by spherical harmonic degree two at the present-day. Such large changes in the non-uniform part of CMB heat flux are not expected if the pattern of lower mantle heterogeneity were to remain fixed. Accordingly, for the dynamo in this study with tomographic forcing we assume that (1) derived from the present-day seismic structure holds everywhere on the CMB at all times, and for this dynamo we assume that the total CMB heat flow is constant at all times.

4. Core evolution

We calculate the evolution of the core structure, temperature and composition as controlled by the total flow at the CMB assuming that the outer core is well-mixed and adiabatic, the inner core boundary (ICB) is at the melting point, and using the radius of the inner core $r_{icb}(t)$ as the progress variable. The conservation of energy for the core can be written as

$$Q_{\rm cmb} = Q_s + Q_l + Q_g + Q_r, \tag{2}$$

where $Q_{\rm cmb}$ is the total heat flow at the CMB, Q_s the secular cooling of the core, Q_l the latent heat released by inner core solidification, Q_g the gravitational energy dissipated through the redistribution of the light elements – O, Si, S, C, etc. – that are partitioned into the outer core by inner core crystallization, and Q_r is the radioactive heat production in the core (Buffett et al., 1996; Labrosse, 2003; Gubbins et al., 2004; Nimmo, 2007). We assume that $Q_{\rm cmb}$ in (2) is imposed on the core by mantle convection, and controls the rate of cooling of the core and the rate of inner core solidification.

In evaluating (2) it is convenient to represent the basic state density ρ, gravity g, melting temperature T_m, and temperature T of the core in terms of analytical functions of the radius. Using the logarithmic equation of state of Poirier and Tarantola (1998) and Lindemann's law of melting, Labrosse (2003) obtained the following expressions:

$$\rho = \rho_c \exp\left(-\frac{r^2}{r_\rho^2}\right), \tag{3}$$

$$g = \frac{4\pi}{3}\mathcal{G}\rho_c r\left(1 - \frac{3}{5}\frac{r^2}{r_\rho^2}\right), \tag{4}$$

$$T_m = T_{m0}\exp\left[-2\left(1 - \frac{1}{3\gamma}\right)\frac{r^2}{r_T^2}\right], \tag{5}$$

$$T = T_m(r_{icb})\exp\left(\frac{r_{icb}^2 - r^2}{r_T^2}\right), \tag{6}$$

with

$$r_\rho = \sqrt{\frac{3K_0}{2\pi\mathcal{G}\rho_0\rho_c}\left(\ln\frac{\rho_c}{\rho_0} + 1\right)}, \quad r_T = \sqrt{\frac{3c_p}{2\pi\alpha_c\rho_c\mathcal{G}}}. \tag{7}$$

Here T_{m0} is the melting temperature at the center of the core, r_{icb} the radius of the inner core, γ the Grüneisen coefficient (assumed constant in the core), ρ_0 and ρ_c the density of liquid iron at zero pressure and at the center of the core, K_0 the incompressibility at zero pressure, $\mathcal{G}$ the universal gravitational constant, c_p the heat capacity (assumed constant), and α_c the coefficient of thermal expansion of liquid iron at the center of the core.

As shown by Labrosse (2003), the contributions of secular cooling Q_s, latent heat Q_l, and gravitational energy release Q_g can all be written in the form $Q_i = P_i(r_{\rm icb})\dot{r}_{\rm icb}$, which allows us to express the evolution rate of the inner core radius as

$$\dot{r}_{icb} = \frac{Q_{\rm cmb} - Q_r}{P_l + P_g + P_s}. \tag{8}$$

In the Labrosse (2003) parameterization of the core state, the functions P_i are given by

$$P_l = 4\pi r_{\rm icb}^2 \rho(r_{\rm icb}) T_m(r_{\rm icb}) \Delta S, \tag{9}$$

$$P_g = \frac{8\pi^2}{3}\mathcal{G}\Delta\rho\rho_c r_{\rm icb}^2 r_{\rm cmb}^2 \left(\frac{3}{5} - \frac{r_{\rm icb}^2}{r_{\rm cmb}^2}\right), \tag{10}$$

$$P_s = 4\pi H^3 \rho_c c_p T_{m0}\left(1 - \frac{2}{3\gamma}\right)\frac{r_{\rm icb}}{r_T^2} \times \exp\left[\left(\frac{2}{3\gamma} - 1\right)\frac{r_{\rm icb}^2}{r_T^2}\right] I(H, r_{\rm cmb}), \tag{11}$$

where ΔS is the entropy of melting of iron, $r_{\rm cmb}$ the CMB radius, $\Delta\rho$ is the density difference between inner and outer core due to differences in their light element contents, $H = \left(1/r_\rho^2 + 1/r_T^2\right)^{-1/2}$, and

$$I(H, r_{\rm cmb}) = \frac{\sqrt{\pi}}{2}\,\mathrm{erf}\left(\frac{r_{\rm cmb}}{H}\right) - \frac{r_{\rm cmb}}{H}\exp\left(-\frac{r_{\rm cmb}^2}{H^2}\right). \tag{12}$$

Integrating (8) backward in time from present-day conditions gives $r_{\rm icb}(t)$. Let χ represent light element concentration. Assuming that the outer core is well-mixed, evolution of the average light element concentration in the outer core χ_{oc} can be obtained from the Rayleigh distillation equation as

$$\dot{\chi}_{oc}(t) = \chi_{oc}(1 - D)\frac{dM_{\rm ic}}{M_{\rm oc}} \simeq \chi_{oc}(1 - D)3\frac{r_{\rm icb}^2 \dot{r}_{\rm icb}}{r_{\rm cmb}^3}, \tag{13}$$

where D is the light element inner core/outer core partitioning coefficient, and $M_{\rm ic}$ and $M_{\rm oc}$ the masses of the inner core and outer core, respectively. In this study we assume $D = 0$ for simplicity.

From the equations above we calculate Φ, the work done per unit time by the buoyancy forces in maintaining the core in a well-mixed state, which is approximately

$$\Phi = 4\pi r_{\rm icb}^2 \dot{r}_{\rm icb}\left(\Delta\rho + \frac{\alpha\rho T_m(r_{\rm icb})\Delta S}{c_p}\right)[\psi_{oc} - \psi(r_{\rm icb})] + \frac{\alpha}{c_p}(Q_{\rm cmb} - Q_{\rm ad})[\psi(r_{\rm cmb}) - \psi_{oc}], \tag{14}$$

where ψ is the gravitational potential calculated from (4), ψ_{oc} is the mean gravitational potential of the outer core, and $Q_{\rm ad}$ is the portion of the CMB heat flow conducted down the adiabat (Buffett et al., 1996). In (14), the first term is the sum of the contributions of the buoyancy forces originating from the compositional and latent heat fluxes at the ICB, and the second term is the contribution of the buoyancy forces originating from cooling at the CMB.

Fig. 1 shows the evolution of the core structure and of the ICB and CMB contributions to Φ versus time using $Q_{\rm cmb}(t)$ from mantle reconstruction HF1 by Zhang and Zhong (2011) in which we have used the core parameters listed in Table 1, and for comparison a reference model that uses the same parameters but assumes a constant $Q_{\rm cmb} = 13$ TW. Solidification of the inner core began around 705 Ma according to both models. Fig. 1 shows that for both mantle histories, Φ is dominated by the contribution of the ICB buoyancy flux.

Table 1
Core evolution parameters.

Parameter		Value
Density at core center	ρ_c	12,500 kg m^{-3}
Density at zero pressure	ρ_0	7500 kg m^{-3}
Compositional density jump at the ICB	$\Delta\rho$	500 kg m^{-3}
Incompressibility at zero pressure	K_0	4.75×10^{11} Pa
Melting temperature at the ICB	$T_m(r_{\rm icb})$	5500 K
Grüneisen parameter	γ	1.5
Heat capacity	c_p	850 J kg^{-1} K^{-1}
Thermal expansion coefficient at core center	α_c	1.3×10^{-5} K^{-1}
Compositional expansion coefficient	β	1
Thermal conductivity at the CMB	k	28 W m^{-1} K^{-1}
Density length scale	r_ρ	7400 km
Temperature length scale	r_T	6040 km
ICB radius	$r_{\rm icb}$	1221 km
CMB radius	$r_{\rm cmb}$	3480 km
Outer core light element concentration	χ_{oc}	5.3 wt.%
Mass of the core	M_c	1.95×10^{24} kg
Kinematic viscosity	ν	10^{-6} m^2 s^{-1}

5. Dynamo control parameters

We define the co-density C in terms of the temperature and light element concentration in the outer core as

$$C = \rho_{oc}(\alpha\theta + \beta\chi') \tag{15}$$

where ρ_{oc} is average density, $\alpha = -1/\rho_{oc}(\partial\rho/\partial\theta)$, $\beta = -1/\rho_{oc}(\partial\rho/\partial\chi')$, $\theta = T - T_{\rm ad}$ is the potential temperature, $T_{\rm ad}$ is the time-dependent outer core adiabat anchored at the ICB, and $\chi' = \chi - \chi_{oc}$ is the local deviation in light element concentration from the outer core average. By combining the conservation equations for heat and light elements in the outer core and using the Boussinesq approximation (Jones, 2007), we obtain the co-density equation:

$$\frac{DC}{Dt} = \kappa\nabla^2 C + \rho_{oc}\alpha\left(\frac{h}{c_p} - \dot{\theta}_{oc}\right) - \rho_{oc}\beta\dot{\chi}_{oc}. \tag{16}$$

Here κ is diffusivity (assumed equal for heat and light elements), h is the production of radiogenic heat per unit of mass, c_p is specific heat, and $\dot{\theta}_{oc}$ is defined as

$$\dot{\theta}_{oc} = \frac{\partial T_{\rm ad}}{\partial t} - \kappa\nabla^2 T_{\rm ad}. \tag{17}$$

We non-dimensionalize length by $r_{\rm cmb} - r_{icb} = d$, time by the viscous diffusion time d^2/ν and velocity by ν/d, where ν is kinematic viscosity, and we scale the co-density by $\rho_{oc}\beta d^2\dot{\chi}_{oc}/\nu$. The dimensionless co-density equation becomes

$$\frac{DC}{Dt} = Pr^{-1}\nabla^2 C + \epsilon \tag{18}$$

where $Pr = \nu/\kappa$ is the Prandtl number and

$$\epsilon = -1 - \frac{\alpha\dot{\theta}_{oc}}{\beta\dot{\chi}_{oc}} + \frac{\alpha h/c_p}{\beta\dot{\chi}_{oc}} \tag{19}$$

With the above scalings we have

$$Ek = \frac{\nu}{\Omega d^2}, \quad P_m = \frac{\nu}{\eta}, \tag{20}$$

for the Ekman number and magnetic Prandtl number, where Ω is angular velocity of rotation and $\eta = 1/\mu_0\sigma$ is the magnetic diffusivity, σ and μ_0 being the electrical conductivity and magnetic permeability, respectively.

Consideration of the various buoyancy sources in the outer core leads to four versions of the Rayleigh number, given by

$$Ra_\chi = \frac{\beta g d^5 \dot{\chi}_{oc}}{\nu^2 \kappa}, \quad Ra_q = \frac{\alpha g d^4 (q_{\rm cmb} - q_{\rm ad})}{\nu \kappa k}, \quad Ra_\theta = -\frac{\alpha g d^5 \dot{\theta}_{oc}}{\nu^2 \kappa}, \quad Ra_r = \frac{\alpha g d^5 h}{c_p \nu^2 \kappa}. \tag{21}$$

In terms of these, the sink term in the co-density equation can be written as

$$\epsilon = -1 + \frac{Ra_\theta}{Ra_\chi} + \frac{Ra_r}{Ra_\chi}. \tag{22}$$

$\epsilon = -1$ if the dynamo is purely compositional. The heat flux boundary condition at the CMB in terms of the dimensionless codensity is given by

$$\left.\frac{\partial C}{\partial r}\right|_{\rm cmb} = -\frac{\alpha}{\beta}\frac{\nu(q_{\rm cmb} - q_{\rm ad})}{k d \dot{\chi}_{oc}} = -\frac{Ra_q}{Ra_\chi}. \tag{23}$$

The boundary condition at the ICB is just $C = C_{icb}$.

The different source terms in the co-density equation can be calculated from the core evolution model. The compositional source term is straightforward, $\dot{\chi}_{oc}$ being given by the distillation Eq. (13) in terms of $\dot{r}_{\rm icb}$. Radioactive heating, if included, is calculated by assuming an homogeneous distribution of radioactive elements in the core. The effective heating rate $\dot{\theta}_{oc}$ as defined in (17) is in general a function of radius as well as time. With the parameters used here, $\dot{\theta}_{oc}$ would be up to 35% higher at the ICB than at the CMB, the radial variations being mostly due to the secular cooling term. This radial dependence could be implemented in a dynamo model, but, for the sake of simplicity, we choose here to use average values of these terms,

$$\dot{\theta}_{oc} = \left\langle \frac{\partial T_{\rm ad}}{\partial t} \right\rangle - \left\langle \kappa \nabla^2 T_{\rm ad} \right\rangle, \tag{24}$$

where $\langle \cdots \rangle$ denotes the mass average taken over the whole core. The mean secular cooling is

$$\left\langle \frac{\partial T_{\rm ad}}{\partial t} \right\rangle = -\frac{P_s(r_{\rm icb})}{M_c} \dot{r}_{\rm icb}, \tag{25}$$

where M_c is the mass of the whole core, and P_s is defined in (11). The mean contribution of heat conduction along the adiabat can be calculated as

$$\left\langle \kappa \nabla^2 T_{\rm ad} \right\rangle = \frac{1}{M_c} \int_V \rho \kappa \nabla^2 T_{\rm ad} dV \tag{26}$$

$$= \frac{1}{M_c} \frac{k}{c_p} \int_V \nabla^2 T_{\rm ad} dV \tag{27}$$

$$= 3 \frac{k}{\bar{\rho} c_p r_{\rm cmb}} \left.\frac{\partial T_{ad}}{\partial r}\right|_{\rm cmb} \tag{28}$$

$$= -\frac{6\bar{\kappa}}{r_T^2} T_{\rm ad}(r_{\rm cmb}) \tag{29}$$

where $\bar{\rho}$ is the mean density of the core, and $\bar{\kappa} = k/\bar{\rho} c_p$.

Evolution of the core implies that the following dynamo control parameters are all functions of time (or age): $Ek, Ra_\chi, Ra_\theta, Ra_r, \epsilon$, and $\partial C/\partial r_{\rm cmb}$. The Ekman number Ek is inversely proportional to the angular velocity of rotation Ω or directly proportional to the length of the day. Analyses of growth patterns of fossil shells (Zhao et al., 2007), corals (Wells, 1963), stromatolites (Vanyo and Awramik, 1985) and of tidal rhythmites (Sonett et al., 1996) consistently give a nearly linear increase of the length of the day during the Phanerozoic, at rate of approximately 24 s Myr^{-1} (Williams, 2000), which corresponds to an increase of approximately 3.7 h per day over the past 550 Ma.

The other variable control parameters involve the thermal and compositional state of the core, and their time dependence is determined from the core history. Using the results in Fig. 1 we calculate the time dependence in $Ek, Ra_\chi, Ra_\theta, \epsilon$, and $\partial C/\partial r_{\rm cmb}$, setting $Ra_r = 0$ on the assumption that the radioactive content of the core makes a negligible contribution to its energy balance. We note that a part of the time dependence in the Ek and the Ra-factors comes from the change in outer core thickness $d(t)$ with time as the inner core grows. In calculating the response of the geomagnetic field,

Table 2
Core evolution model HF1.

Age (Ma)	$\frac{r_{\rm ic}}{r_{\rm cmb}}$	$\frac{Ra_\chi}{Ra_\chi(0)}$	$\frac{Ek}{Ek(0)}$	$\partial_r C\|_{\rm cmb}$	$\frac{\partial_r C\|_{\rm cmb}}{\partial_r C(0)\|_{\rm cmb}}$	ϵ	$\frac{\epsilon}{\epsilon(0)}$
0	0.351	1	1	−0.101	1	−0.8005	1
50	0.339	1.121	0.952	−0.1031	1.019	−0.781	0.975
90	0.329	1.167	0.913	−0.1034	1.022	−0.774	0.968
100	0.327	1.207	0.904	−0.1041	1.029	−0.768	0.959
150	0.314	1.200	0.859	−0.1030	1.018	−0.772	0.964
180	0.307	1.222	0.833	−0.1030	1.019	−0.769	0.961
220	0.296	1.275	0.799	−0.1037	1.025	−0.760	0.949
275	0.282	1.330	0.754	−0.1043	1.032	−0.750	0.937
330	0.266	1.468	0.710	−0.1071	1.059	−0.721	0.901

Table 3
Core evolution model with constant CMB heat flux.

Age (Ma)	$\frac{r_{\rm ic}}{r_{\rm cmb}}$	$\frac{Ra_\chi}{Ra_\chi(0)}$	$\frac{Ek}{Ek(0)}$	$\partial_r C\|_{\rm cmb}$	$\frac{\partial_r C\|_{\rm cmb}}{\partial_r C(0)\|_{\rm cmb}}$	ϵ	$\frac{\epsilon}{\epsilon(0)}$
0	0.351	1	1	−0.1007	1	−0.804	1
50	0.339	1.067	0.952	−0.1025	1.006	−0.785	0.988
110	0.324	1.156	0.894	−0.1038	1.015	−0.769	0.971
150	0.314	1.218	0.859	−0.1043	1.023	−0.761	0.959
180	0.307	1.265	0.833	−0.1046	1.029	−0.755	0.949
220	0.296	1.331	0.799	−0.1053	1.038	−0.746	0.935
275	0.282	1.425	0.754	−0.1064	1.053	−0.733	0.914
330	0.266	1.526	0.710	−0.1079	1.071	−0.714	0.889
400	0.243	1.674	0.653	−0.1113	1.105	−0.678	0.844
475	0.214	1.849	0.592	−0.1170	1.161	−0.622	0.774
550	0.179	2.026	0.530	−0.1268	1.260	−0.529	0.658
660	0.102	2.077	0.426	−0.1779	1.766	−0.082	0.102
770	0	0	0.331	–	–	–	–

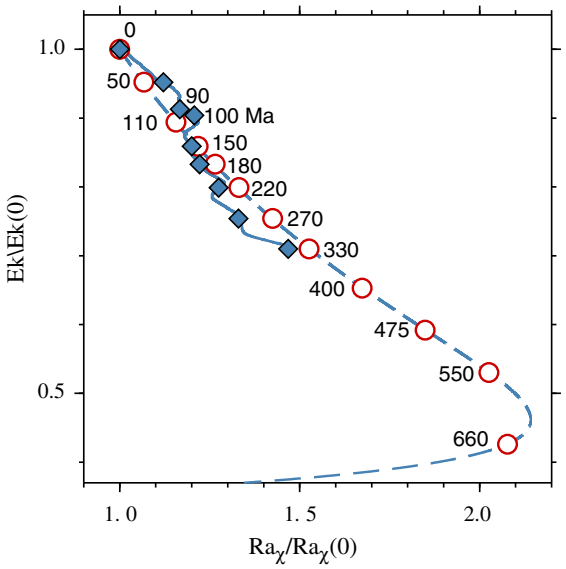

Fig. 2. Core evolution from Fig. 1 expressed in terms of the time variation in the Ekman number and Rayleigh number relative to present-day values. Solid line with diamonds is core evolution driven by mantle history HF1 with time variable CMB heat flow; dashed line with circles is core evolution driven by constant CMB heat flow. Numbers indicate ages in Ma.

we are mostly interested in the changes in the dynamo control parameters relative to their present-day values. Tables 2 and 3 give the ratios of the main dynamo control parameters at various stages relative to the present-day based on the core-evolution models and Fig. 2 shows the change in the Rayleigh number Ra_χ versus Ekman number Ek for the two types of mantle evolution.

6. Phanerozoic dynamo simulations

Numerical dynamos have been run continuously for the equivalent of about 200 Myr with fixed values of the control parameters and fixed boundary conditions by Wicht et al. (2009) and with time dependent values of the control parameters and time dependent boundary conditions by Driscoll and Olson (2011). Each of these long continuous simulations produced more than one hundred reversals. The non-evolving dynamo by Wicht et al. (2009) included both short and long stable polarity chrons, with the histogram of chron lengths approximating a Poisson distribution. However, it did not produce extremely long constant polarity (superchron-type) states, and its reversal sequence did not show the long period cycling seen in the GPTS. In contrast, the long dynamo simulation by Driscoll and Olson (2011) produced a 200 Myr variation in reversal frequency including superchrons by modulating the strength of outer core convection through prescribed, periodic variations in the co-density flux at the CMB. In their simulation, constant polarity superchrons corresponded to times when CMB heat flow was minimum whereas frequent reversals occurred when CMB heat flux was maximum. Neither of these two long dynamo simulations included variations in the rotation rate or lateral heterogeneity in the CMB heat flow, both of which are known from previous studies to affect dynamo reversal stability (Glatzmaier et al., 1999; Kutzner and Christensen, 2004; Driscoll and Olson, 2009a; Olson et al., 2010).

Rather than attempt to reproduce the entire GPTS in a continuous dynamo simulation, we focus in this study on selected times of about 5.45 Myr duration. This choice of time duration is based partly on practical considerations. It is long enough that the average reversal rate can be estimated, yet short enough that we can neglect the evolution of the core and mantle within each simulation. The nominal Phanerozoic time periods we simulate include the present-day (0–5 Ma), early Eocene (50 Ma), mid-Cretaceous (100 and 110 Ma), early Jurassic (180 Ma), late Triassic (220 Ma), early-middle Permian (275 Ma), Mississippian (330 Ma), early-middle Ordovician (475 Ma) and near the Cambrian-Precambrian boundary (550 Ma). We also calculate HF1 dynamo reversals in the Cretaceous at 90 Ma and in the late Jurassic at 150 Ma. In terms of geomagnetic history, 0–5, 150, 180, 220 and 330 Ma represent times with relatively frequent reversals, and 100, 275, and 475 Ma represent constant polarity superchrons or times with large polarity bias and infrequent reversals. In terms of mantle history, 100 Ma was a time of continent dispersion and high sea level (Cognè and Humler, 2004; Miller et al., 2005), 180 Ma marks the breakup of Pangaea, 275 Ma marks the height of Pangaea with continental glaciation (Eyles, 1993), 330 Ma coincides with Pangaea assembly (Torsvik and Cocks, 2004), and 475 Ma represents a time with dispersed continents (Cocks and Torsvik, 2002).

Our procedure is to determine dynamo control parameters that yield the present-day (0–5 Ma) average reversal rate, then vary the values of these control parameters and the CMB and ICB boundary conditions according to Tables 2 and 3 to calculate dynamo behavior at the earlier times. One advantage of this approach is that it highlights the relative changes in geomagnetic field behavior that are attributable to core-mantle evolution. A potential weakness is that the results depend sensitively on the choice of the dynamo used for the present-day.

As discussed earlier, two models of CMB heat flow heterogeneity are used, one being the CMB heat flow heterogeneity predicted by the Zhang and Zhong (2011) HF1 mantle history, the other derived from the present-day lower mantle seismic tomography. For both dynamos, the CMB heat flow heterogeneity is converted to CMB co-density flux in the numerical dynamo using the proportionality

$$\delta c/\bar{c} = \delta q/\bar{q} \tag{30}$$

where q is the local CMB heat flux, $c = \partial C/\partial r_{cmb}$ is the local co-density flux at the CMB, the overbars represent CMB averages, and δ represents deviations from the CMB averages. Before applying (30) we subtract the heat flow down the core adiabat in $\bar{q}$ and we subtract the subcritical conductive gradient in $\bar{c}$, that is, the difference between the critical conductive gradient for the onset of convection and the adiabatic gradient. The first of these corrections is necessary because the numerical dynamo uses the Boussinesq approximation and therefore assumes zero adiabatic temperature gradient, whereas the adiabatic temperature gradient in the core is large. The second correction is necessary because the subcritical conductive gradient in the numerical dynamo is large, whereas it is negligible in the core.

To specify the present-day thermal state of the core, we use $\epsilon = -0.8$ and $\bar{c} = -0.1$ for the CMB average co-density gradient as dictated by the present-day core energy balance described in the previous section. For the present-day outer core dynamics we choose $Pr = 1, Pm = 20$ and $Ek = 5.75 \times 10^{-3}$. We then systematically vary the strength of outer core convection by adjusting Ra_χ in the numerical dynamo, calculating the time average magnetic field structure and reversal frequency and comparing these with the present-day geomagnetic field at the CMB and with the 0-5 Ma geomagnetic reversal rate to find the best present-day Ra_χ-value. Results of this procedure applied to the present-day HF1 dynamo are given in Table 4. In Table 4 and elsewhere in this paper we use the Elsasser number scale factor $(\rho_{oc}\Omega/\sigma)^{1/2}$ to nondimensionalize magnetic field intensity. Dynamo reversal rate comparisons with the GPTS use magnetic field diffusion time scaling based on the dipole free decay time

$$\tau = \frac{r_{cmb}^2}{\pi^2 \eta}. \tag{31}$$

For the core, we assume $\tau \simeq 20$ kyr. Table 4 also gives the magnetic Reynolds number

$$Rm = \frac{Ud}{\eta} \tag{32}$$

where U is the time average of the rms velocity in the fluid outer core, as well as the local Rossby number

$$Ro_l = \frac{Ul}{\pi d^2 \Omega} \tag{33}$$

where l is the length scale of the convection (Christensen and Aubert, 2006). For dynamo HF1, a Rayleigh number of $Ra_\chi = 3 \times 10^4$ gives $Rm = 166$ and an average reversal frequency of 3.7 Myr^{-1} measured in terms of the 20 kyr dipole decay time, which is comparable

Table 4
HF1 dynamo sensitivity.

Ra_χ	Duration ($\times\tau$)	Dipole intensity (rms)	Reversals	Rm (rms)	Ro_l (rms)
1.5×10^4	100	0.92 ± 0.05	0	79	0.030
2.0×10^4	120	0.84 ± 0.16	0	104	0.038
2.5×10^4	60	0.70 ± 0.23	2	134	0.048
3.0×10^4	273	0.58 ± 0.28	20	166	0.058
3.5×10^4	60	0.50 ± 0.26	6	187	0.067
4.0×10^4	60	0.42 ± 0.27	8	208	0.076

Table 5
Numerical dynamo statistics.

Dynamo	Reversals [Excursions]	Polarity Bias	Dipole Intensity (rms)	Rm (rms)	Ro_l (rms)
HF1 present-day	20 [2]	−0.082	0.577 ± 0.284	166	0.057
HF1 50 Ma	12 [4]	0.274	0.562 ± 0.279	175	0.056
HF1 90 Ma	13 [5]	0.397	0.657 ± 0.271	164	0.051
HF1 100 Ma	23 [19]	0.120	0.368 ± 0.297	190	0.058
HF1 100 MaLQ	4 [2]	0.942	0.672 ± 0.246	149	0.044
HF1 100 MaLQSH	0 (S)	1.00	0.721 ± 0.236	136	0.038
HF1 150 Ma	12 [4]	0.00	0.595 ± 0.289	176	0.053
HF1 180 Ma	20	−0.125	0.725 ± 0.266	171	0.047
HF1 220 Ma	22 [3]	−0.01	0.670 ± 0.302	176	0.046
HF1 275 Ma	0 [1]	−1.00	0.710 ± 0.254	165	0.041
HF1 330 Ma	6 [2]	−0.215	0.731 ± 0.253	178	0.045
HF1 475 Ma	0	1.000	0.568 ± 0.221	190	0.034
Y22 550 Ma	2 [2] (S)	0.765	0.528 ± 0.300	215	0.040
Tomo present-day	23 [16]	−0.013	0.566 ± 0.250	173	0.063
Tomo 50 Ma	15 [8]	−0.212	0.605 ± 0.247	174	0.057
Tomo 110 Ma	16 [4]	0.262	0.632 ± 0.255	182	0.056
Tomo 110 MaSH	8	0.628	0.649 ± 0.239	181	0.055
Tomo 180 Ma	16 [2]	0.327	0.644 ± 0.263	173	0.052
Tomo 220 Ma	17 [7]	0.339	0.590 ± 0.281	190	0.053
Tomo 275 Ma	18	−0.055	0.630 ± 0.290	193	0.050
Tomo 330 Ma	35 [10]	−0.030	0.561 ± 0.328	207	0.048
Tomo 475 Ma	11 [6]	−0.362	0.591 ± 0.264	204	0.043

HF1 = CMB heat flux from Zhang and Zhong (2011) mantle history; Tomo = CMB heat flux from lower mantle tomography; Y22 = spherical harmonic degree, order 2 heterogeneity Duration = 272.5τ, S = 100τ; Dipole intensity is time average rms in dimensionless Elsasser number units on CMB; LQ = low CMB heat flow dynamo; SH = small CMB heterogeneity dynamo; Dipole intensity, Rm and Ro_l are time averages of rms.

to the 0–5 Ma GPTS reversal frequency of 4 Myr^{-1}. The same procedure applied to the tomographic dynamo with $Ra_\chi = 3.15 \times 10^4$ yields an average reversal rate of 4.2 Myr^{-1} and $Rm = 173$ for the present-day. Statistics for these present-day cases are given in Table 5 along with statistics at earlier times, including the number of reversals, the time average polarity bias defined by

$$\mathcal{B} = \frac{t_N - t_R}{t_N + t_R} \tag{34}$$

where t_N and t_R denote the times spent in normal and reverse polarity, the time average and the standard deviation of the rms dipole intensity on the CMB in non-dimensional units, and time averages of Rm and Ro_l. All the results in Tables 4 and 5 were calculated using the open source dynamo code MAG available at www.geodynamics.org with 33 radial grid points and 32 spherical harmonics for the angular resolution.

Driscoll and Olson (2009b) showed that the dipole intensities of dynamos with control parameters similar to the present-day cases in Tables 4 and 5 can be scaled to the present-day geomagnetic dipole intensity within a factor of about two, and Aubert et al. (2009) have shown that the same scaling applies to dipole intensities in the past, when the inner core was smaller. For reversals, it is well established that the transition to reversing behavior and the frequency of reversals in numerical dynamos depend on the control parameters as well as the CMB heterogeneity (Glatzmaier et al., 1999; Kutzner and Christensen, 2004; Olson et al., 2010). Although there is no agreement on how best to extrapolate this behavior to the geodynamo, there are several proposals. Petrelis et al. (2011) argue that reversal frequency is best parameterized in terms of the symmetry of the mantle forcing, which presumably includes the symmetry of CMB heat flow, whereas others have argued that the transition to reversals is best parameterized in terms of the dynamo control parameters (Christensen and Aubert, 2006).

Fig. 3 shows the domain of magnetic Reynolds numbers Rm and magnetic Ekman numbers

$$Ek_\eta = \frac{\eta}{\Omega d^2} \tag{35}$$

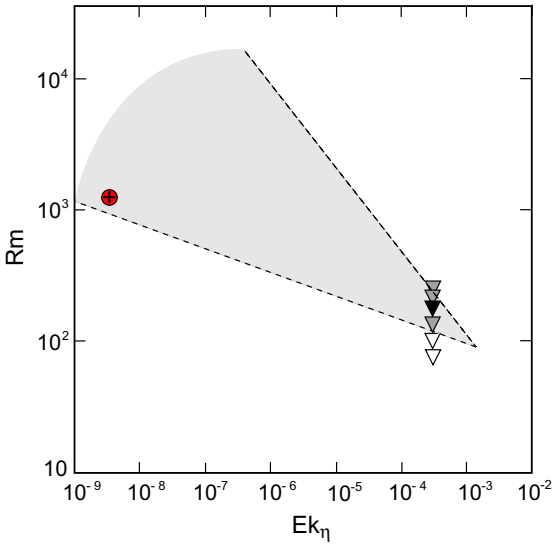

Fig. 3. Magnetic Reynolds number versus magnetic Ekman number for dynamos with present-day mantle structure from Table 4 (triangles) compared with present-day geodynamo (circle). Triangle shades indicate dynamo reversal behavior (shaded = reversing, unshaded = non-reversing, black = present-day reversal rate). Light grey denotes the region of Earth-like dynamo behavior determined by Christensen et al. (2010) with a lower bound corresponding to the power law (36).

from numerical dynamos that Christensen et al. (2010) deemed to be "Earth-like" in terms of their magnetic field structure and secular variation, excluding reversals. The present-day geodynamo is found to lie just above the lower boundary of the domain, which is defined by the power law relationship

$$Rm \simeq 27 Ek_\eta^{-2/11} \tag{36}$$

Numerical dynamos lying below the lower boundary in Fig. 3 are more symmetric and less variable than the geodynamo and therefore are presumed to reverse less often or not at all, whereas numerical dynamos lying above the upper boundary are too variable and less dipolar than the geodynamo. Note that the reversing HF1 dynamos from Table 4 lie inside or above the Earth-like domain in Fig. 3 and the non-reversing cases lie below. This association suggests that (36) might represent a lower bound for the transition from reversing to non-reversing behavior. If so, the fact that the geodynamo lies close to (36) is significant, because it implies that only a moderate decrease in Rm would be needed to bring the geodynamo into a non-reversing (i.e., superchron) state, as with our numerical dynamos. Later we examine (36) as a reversal criterion, as well as another proposal by Christensen and Aubert (2006) that reversal scaling depends on the local Rossby number (33).

7. Present-day dynamo structure and reversal sequence

Fig. 4 shows the heat flux pattern on the CMB and the corresponding time average magnetic field on the CMB at the present-day from mantle history HF1 and for tomographic forcing, respectively. The HF1 CMB heat flux has been truncated at spherical harmonic degree 4 and the tomographic heat flux has been truncated at spherical harmonic degree 3. The present-day HF1 and tomographic CMB heat flux patterns are quite similar, both dominated by spherical harmonic degree two variations, with sector-shaped maxima beneath east-central Asia and the Americas, marking the locations of major mantle downwellings, and minima beneath Africa and the central Pacific, marking the large seismic low velocity provinces, which are thought to represent compositionally dense

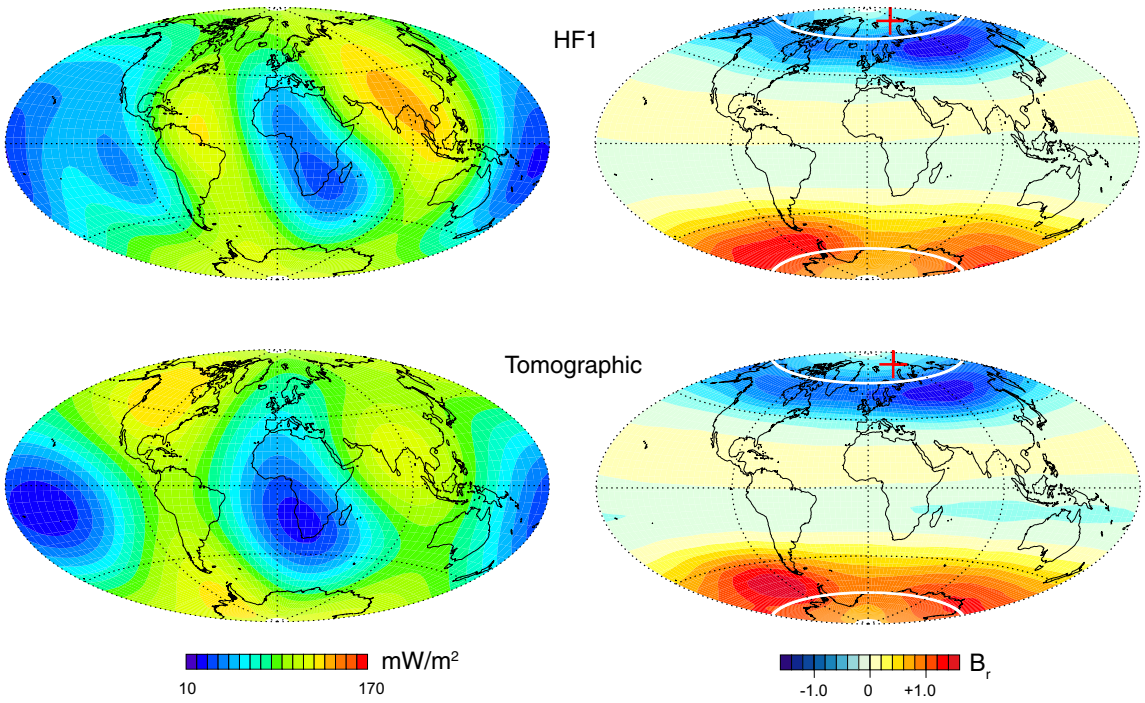

Fig. 4. Comparison of present-day CMB heat flux (left) and the corresponding time average dynamo radial magnetic field on the CMB during normal polarity times (right). HF1 = CMB heat flux from mantle history HF1 with spherical harmonic degree $l = 4$ truncation; Tomographic = CMB heat flux from lower mantle tomography with spherical harmonic degree $l = 3$ truncation. Magnetic intensity contours are in dimensionless Elsasser number units, red crosses mark the geomagnetic pole, white curves mark the inner core tangent cylinder.

piles at the base of the mantle (McNamara and Zhong, 2005; Burke, 2011).

The time average magnetic fields from the two dynamos are also nearly the same for the present-day. In both dynamos, two patches of high intensity radial magnetic field are present in each hemisphere, located approximately at the longitudes where the CMB heat flux has its maxima. Comparable high field intensity patches are present in the historical geomagnetic field on the CMB at approximately these same locations (Jackson et al., 2000). According to numerical dynamo results, these high intensity patches result from concentration of the magnetic field at major downwellings in the outer core, which tend to form where the CMB heat flux is high (Kutzner and Christensen, 2004). Fig. 4 shows the time average magnetic field structure during normal polarity times; apart from the change in sign, the pattern is essentially the same during reverse polarity times. The time average fields are dipole dominant, and except for the high intensity patches, they are nearly axisymmetric. In each dynamo, however, the magnetic patches beneath Siberia and the tip of South America are slightly stronger than the other two, which tilts the axis of the time average dipole in the direction of the stronger patches and away from the weaker ones. This patch asymmetry produces a time average dipole tilt of about 10° in both dynamos, which is comparable to the 5–12° dipole tilt in the historical geomagnetic field (Jackson et al., 2000), but larger than the average dipole tilt of less than 5° inferred for the archaeomagnetic field (Korte et al., 2011) and for the 0–5 Ma paleomagnetic field (Johnson and Constable, 1995).

Fig. 5 shows time series of the magnetic dipole field intensity on the CMB and the polarity reversal sequence for the two dynamos, driven by their respective present-day CMB heat flux patterns, compared with the 0–5 Ma GPTS and 0–2 Ma relative paleointensity from SINT2000 (Valet et al., 2005). Fig. 5a is from the dynamo with CMB heat flux derived from mantle history HF1, and Fig. 5b is from the dynamo driven by CMB heat flux derived from lower mantle seismic tomography. The time axis units are multiples of the dipole free decay time, and assuming $\tau = 20$ kyr in the core, the time span in Fig. 5 is equivalent to about 5.45 Myr. Fig. 5c shows the 0–5 Ma GPTS with the same time scaling. The large amplitude fluctuations of the dipole field intensity in the two numerical dynamos are analogous to the low frequency secular variation in the SINT2000 relative paleointensity record obtained from marine sediments (Valet et al., 2005). These magnetic fluctuations are anti-correlated with fluctuations in the kinetic energy of the convection, so that the fluid velocity is high when the dipole is weak and vice-versa. Polarity reversals and the short polarity events in these dynamos are related to the dipole fluctuations and occur at times when the dipole field is particularly weak, due to the transfer of magnetic energy from the dipole to higher multipole fields (Olson et al., 2009). The polarity reversals in Fig. 5 occur after the dipole field collapses to near zero intensity, so that the relative standard deviation (the ratio of standard deviation to the mean of the dipole intensity) σ^* can be used as a rough proxy for reversal frequency. Table 5 shows that $\sigma^* = 0.49$ for the present-day HF1 dynamo and $\sigma^* = 0.44$ for the present-day tomographic dynamo. These are somewhat greater than $\sigma^* \simeq 0.32$ from the SINT2000 paleointensity record for the past 2 Ma (Valet et al., 2005) although that record may be contaminated by nondipole field components during times of low intensity. The frequency of dipole minima in the two dynamos (measured on the basis of a 20 kyr dipole decay time) is similar to the SINT2000 paleointensity record. In Fig. 5, the frequency of dipole minima, defined as the number of times the dipole intensity falls below one standard deviation of its mean value, is approximately 10 Myr^{-1} for the HF1 dynamo and 13 Myr^{-1} for the tomographic dynamo, compared to an average rate of 13 Myr^{-1} for the SINT2000 record.

Fig. 5 and Table 5 shows that the present-day HF1 dynamo produced 20 reversals and 2 short polarity events in the simulated time, corresponding to an average reversal rate of 3.7 Myr^{-1}, assuming that $\tau = 20$ kyr is the dipole decay time in the core. The present-day tomographic dynamo produced 23 reversals over the

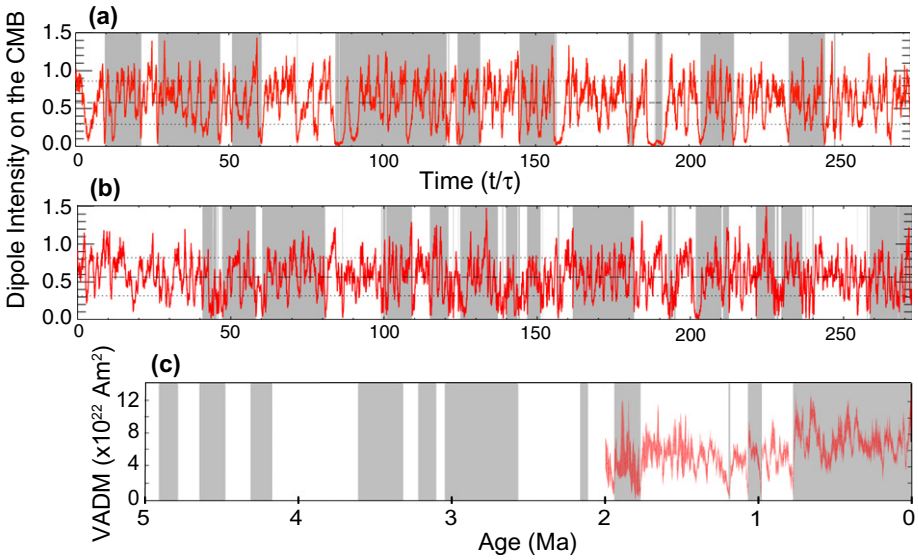

Fig. 5. Comparison of present-day dynamos with paleomagnetic data based on 20 kyr dipole free decay time for the core. (a) Dipole intensity and polarity reversal sequence from the present-day HF1 dynamo. The rms dipole intensity is in dimensionless Elsasser number units; normal and reverse polarity are indicated by shaded and unshaded, respectively. (b) Same for the present-day tomographic dynamo. (c) 0–5 Ma GPTS reversal sequence from Ogg (2012) and 0–2 Ma SINT2000 virtual axial dipole moment (VADM) from Valet et al. (2005).

same time, corresponding to an average rate of 4.2 Myr^{-1} in the core. The tomographic dynamo produced more short, excursion-like events than dynamo HF1, but otherwise the two present-day dynamos yield reversal rates comparable to the 0–5 Ma GPTS average rate of about 4 Myr^{1}. Comparing other statistics in Table 5, both of the present-day dynamos have negative but somewhat smaller polarity biases than the GPTS, with $\mathcal{B} = -0.082$ and -0.014 for HF1 and the tomographic dynamo, respectively, versus $\mathcal{B} = -0.1$ for the 0–5 Ma GPTS.

8. Phanerozoic reversal sequences

Figs. 6 and 7 show time series of dipole intensity and polarity sequences for both dynamos at the Phanerozoic times in Table 5 and Fig. 8 compares reversal rates and polarity bias of both dynamos to the GPTS. To insure smooth evolution of dynamo HF1, the CMB heat flux heterogeneity was truncated at spherical harmonic degree 4 and the CMB patterns at 50, 90, 150 and 220 Ma were interpolated from the other times in Table 5.

Initially, the reversal frequency in both dynamos decreases with age, to 2.2 Myr^{-1} in the HF1 dynamo and 2.75 Myr^{-1} in the tomographic dynamo at 50 Ma, which Fig. 8 shows are just slightly higher than the GPTS at that age. However, this initial decrease is not sustained, as the reversal rate begins to increase beyond 50 Ma in both dynamos, contrary to the trend in the GPTS. At 100 Ma, mantle history HF1 produced a total of 23 polarity reversals for an average rate of 4.2 Myr^{-1}, and the tomographic dynamo at 110 Ma reversed polarity 16 times, for an average rate of 2.9 Myr^{-1}. Both represent significantly different behavior compared to the GPTS during Cretaceous Superchron (CNS). The mean CMB heat flux in mantle history HF1 is 90.8 mW/m^2 at 100 Ma, due to the overall higher mantle convection velocities in HF1 at 100 Ma (Zhang and Zhong, 2011) induced by the high spreading rates in the Lithgow-Bertelloni and Richards (1998) plate tectonic reconstruction at that time. Although the equatorial mean heat flow at 100 Ma is actually somewhat lower than for the present-day in model HF1, the higher total CMB heat flow results in a weaker dipole field at 100 Ma (see Table 5) and a corresponding larger $\sigma^* = 0.8$ compared to the present-day. Fig. 6 shows that the dipole field tends to sputter, spending lengthy periods of time at low intensity in a multipolar field configuration, with high dipole intensities limited to relatively short-lived bursts. In order to verify that the presence of reversals during this period does not depend on the particular time snapshot chosen, we calculated the HF1 dynamo at 90 Ma, when the CMB heat flow was slightly less than at 100 Ma. As Table 5 shows, the HF1 dynamo reversed less often at 90 Ma compared to 100 Ma and it also showed a significant polarity bias, yet it remained far from superchron conditions.

Both mantle histories fail to produce superchron conditions at times corresponding to the CNS, although for somewhat different reasons. For mantle history HF1 the total CMB heat flow is too high at this time, whereas for the tomographic dynamo the CMB heat flux heterogeneity is too large. To demonstrate the sensitivity to these effects, we recalculated the reversal sequence for both dynamos, reducing the total CMB heat flow in HF1 at 100 Ma by 20% in one case, reducing the amplitude of the CMB heat flux heterogeneity at 110 Ma in the tomographic dynamo by 50% in a second case, and reducing both the total heat flow and the heterogeneity amplitude in HF1 by these amounts in a third case. The statistics of these modified dynamos are given in Table 5 and compared with the GPTS in Fig. 8. The dipole fluctuations and the reversal frequency are reduced by these changes and the polarity bias is substantially increased in each case, but only the third case yields stable polarity. Accordingly, we infer that lower total heat flow and lower heat flux heterogeneity compared to either HF1 or tomographic forcing are needed to produce the non-reversing conditions during the CNS. We note that Heller et al. (1996) and Rowley (2002) have both argued for reduced spreading rates around 100 Ma, which might have the desired effect of reducing both the CMB heat flow and its heterogeneity.

Unlike the mid Cretaceous, both mantle histories produce reversal rates and polarity biases earlier in the Mesozoic that are similar to the GPTS. The reversal sequences at 180 Ma in Figs. 6 and 7 yield average rates near 3.8 and 3 Myr^{-1}, respectively, and dynamo HF1 yields an average reversal rate of 2.2 Myr^{-1} at 150 Ma. Fig. 8 shows that these reversal rates are comparable to the average of the GPTS between 120 and 200 Ma, although neither of these dynamos is quite as variable as the GPTS. In particular, neither dynamo shows evidence for the very short chrons (hyper-reversing behavior) seen in the GPTS between 160 and 170 Ma.

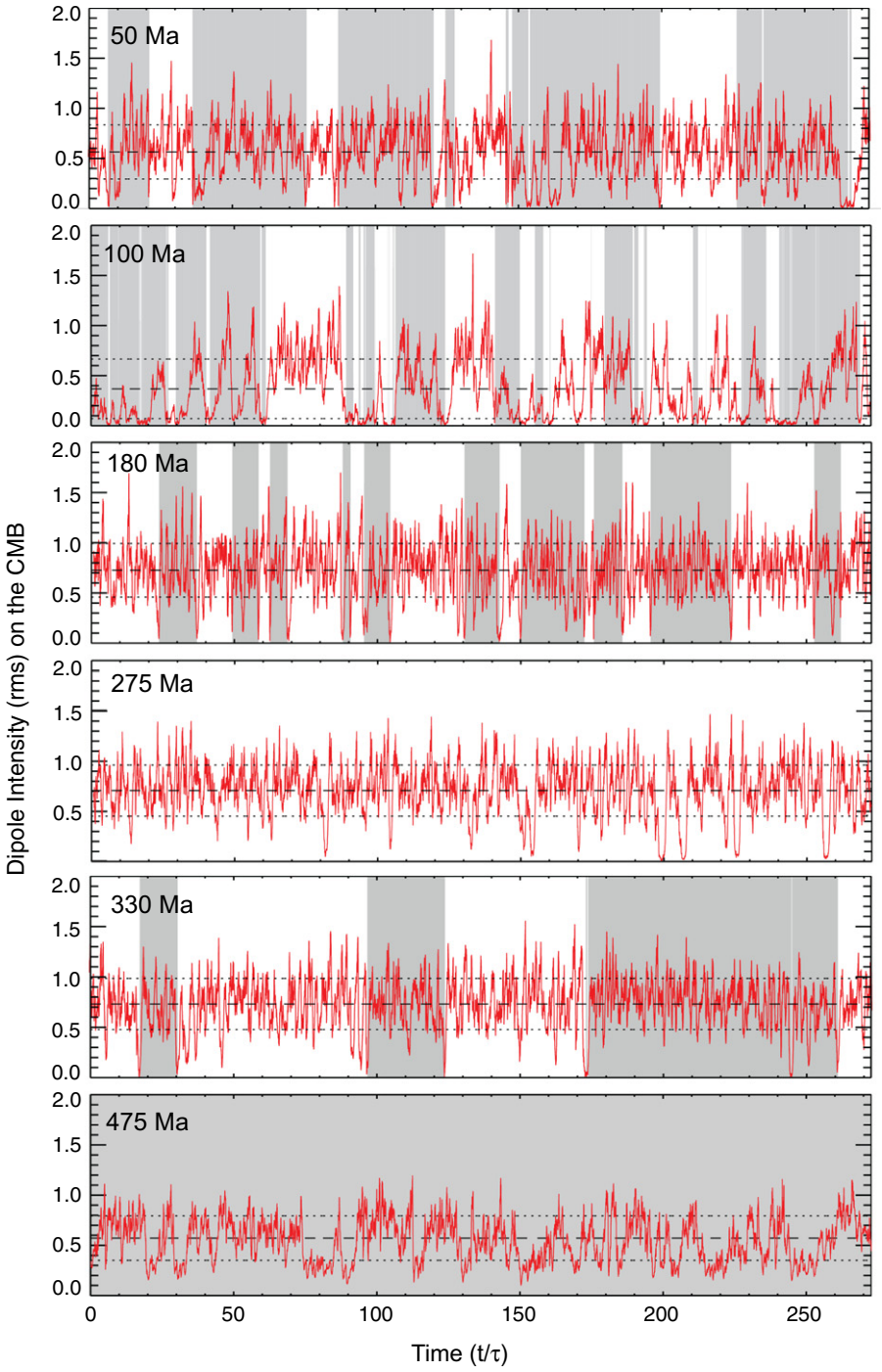

Fig. 6. Polarity reversal sequences and dipole intensity on the CMB in dimensionless Elsasser number units from the HF1 dynamo at various ages. Normal and reverse polarity indicated by shaded and unshaded, respectively. Time axis is in units of dipole free decay; the time span corresponds to approximately 5.45 Myr in the core.

More systematic differences between the two mantle histories become evident with increasing age. At 220 Ma the reversal rates in both dynamos are practically unchanged from 180 Ma, but as Figs. 6 and 8 show, at 275 Ma the HF1 dynamo is very close to non-reversing condition, whereas the tomographic dynamo continues to reverse frequently. Except for a small number of short excursion-like events, the HF1 dynamo at 275 Ma maintained a strong dipole in reverse polarity for the entire 272.5 dipole decay times, although it exhibited numerous dipole collapse events. In order to get a picture of its longer-term reversal potential, we continued this case until the first successful reversal at 530 dipole decay times, at which point the simulation was terminated. On this basis we infer that the HF1 dynamo is very close to superchron conditions at a time that corresponds to the Permian Kiaman Reversed Superchron (KRS) in the GPTS. The polarity stability at this time is a consequence of the combined effects of the relatively low average CMB heat flux, the more rapid rotation, and also the stability provided by the pattern of CMB heterogeneity associated with the Pangaea supercontinent. The qualitative differences between the two dynamos at 275 Ma persist to earlier times. At 330 Ma, the HF1 dynamo reversal frequency is approximately 1.1 Myr^{-1}, comparable to the GPTS, whereas Figs. 7 and 8 show that the tomo-

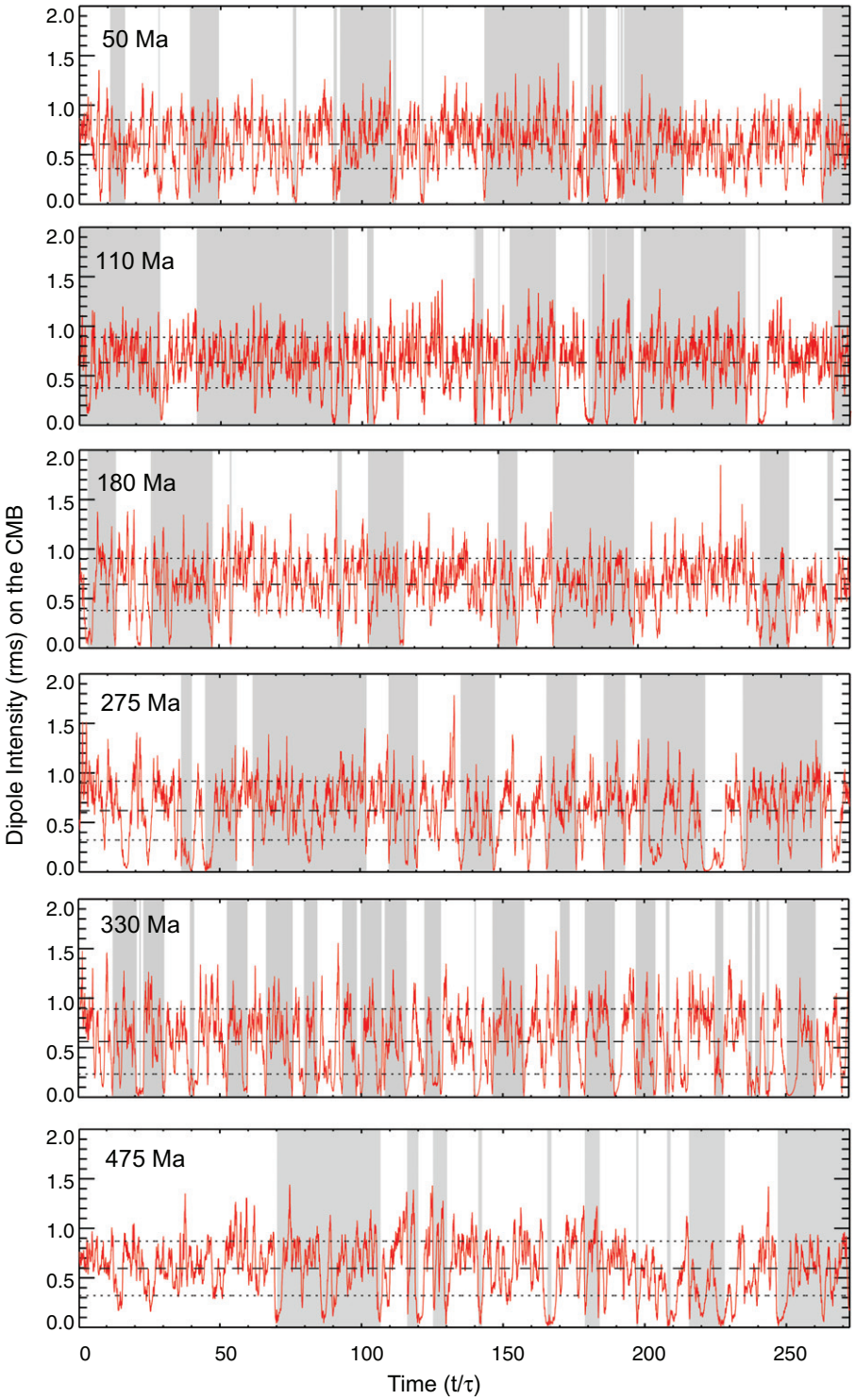

Fig. 7. Polarity reversal sequences and dipole intensity on the CMB in dimensionless Elsasser number units from the tomographic dynamo at various ages. Normal and reverse polarity indicated by shaded and unshaded, respectively. Time axis is in units of dipole free decay; the time span corresponds to approximately 5.45 Myr in the core.

graphic dynamo polarity was less stable, featuring a very high reversal frequency of about 6.4 Myr^{-1} along with numerous shorter polarity events.

Going back still farther into the Phanerozoic, we extrapolated the HF1 dynamo to 475 Ma, corresponding to the Moyero ~~Normal~~ Superchron (M~~N~~S), using the dynamo control parameters from Fig. 2 for this time with the CMB heat flux heterogeneity used for HF1 at 330 Ma. Fig. 6 shows this combination of factors produced stable polarity, whereas Fig. 7 shows the tomographic dynamo continued to reverse, although at a reduced rate of 2 Myr^{-1}. The only difference in the two dynamos at this time is their CMB heat flux heterogeneity. We also constructed a dynamo for the earliest Phanerozoic at 550 Ma using the control parameters from Fig. 2 plus with a spherical harmonic degree and order 2 heat flux heterogeneity. The Y22 CMB heterogeneity is a generic representation of lower mantle hetrogeneity during continent dispersion, and for all

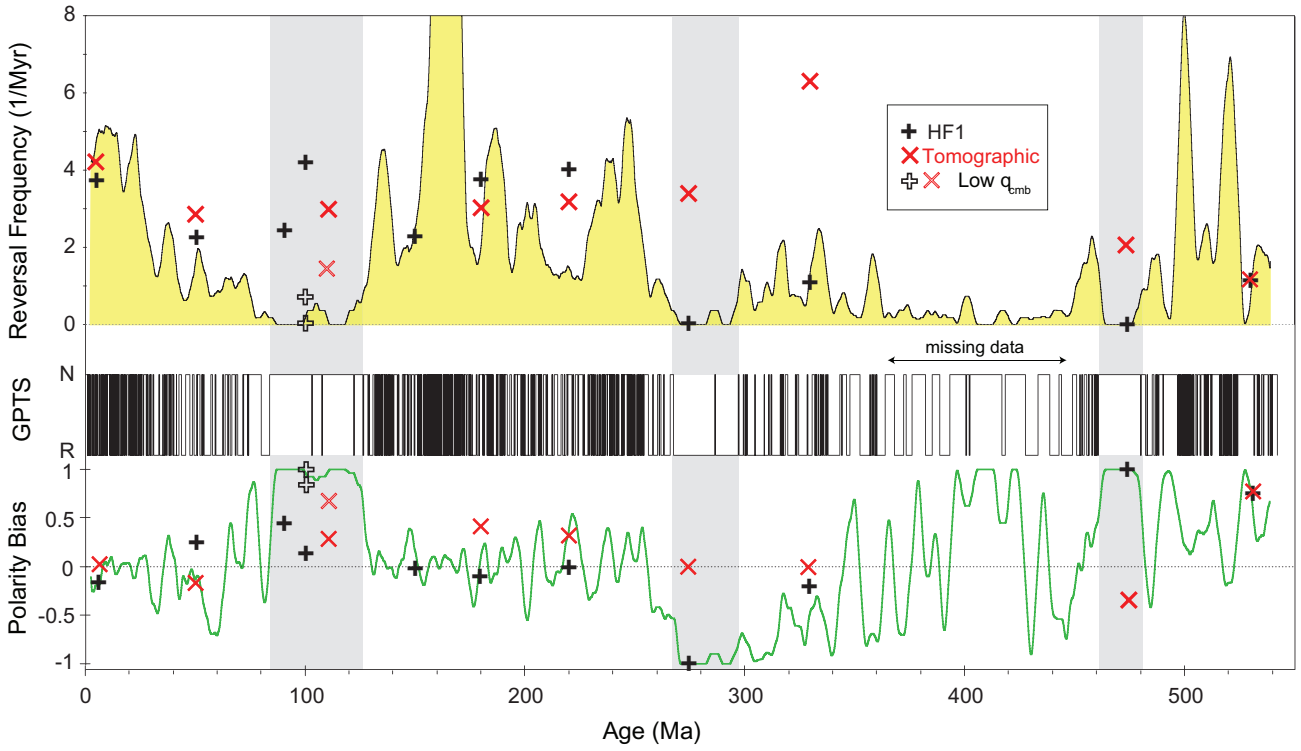

Fig. 8. Top: Comparison of numerical dynamo reversal frequency (symbols) and GPTS reversal frequency. Constant polarity superchrons shown in grey. Middle: GPTS polarity record from Ogg (2012), N = normal, R = reverse polarity. Bottom: comparison of numerical dynamo polarity biases (+, x symbols) and GPTS polarity bias (solid curve). Filled (+, x) symbols denote HF1 and tomographic dynamos, respectively. Unfilled (+, x) symbols denote modified, low CMB heat flux dynamos. GPTS reversal frequencies and polarity biases are 5 Myr averages.

we know, equally applicable to either mantle history, so we denote this dynamo in Fig. 8 using both HF1 and tomographic symbols. It was run for only 100 dipole decay times because of the severe time step constraints imposed by the small inner core, but nevertheless produced reversals at an average rate near 1 Myr^{-1}, roughly comparable to the GPTS.

In summary, we find that the relatively small deviations from monotonic thermal evolution of the core in the Phanerozoic implied by the convective mantle history HF1 produces a slow cycle in reversal frequency in a numerical dynamo tuned to the present-day conditions, with superchron-like conditions around 275 Ma at the time of Pangaea and possibly also at 475 Ma, with relatively frequent reversals at other times. An otherwise similar dynamo with monotonic core evolution driven by a fixed tomographic CMB heat flux pattern derived from the present-day lower mantle seismic heterogeneity fails to produce the same cycling, especially around the time of Pangaea. Although neither mantle history produces superchron-like conditions at the time of the CNS, we find that relatively moderate reductions in the average CMB heat flux and its heterogeneity could produce non-reversing behavior at this time in either of these dynamos.

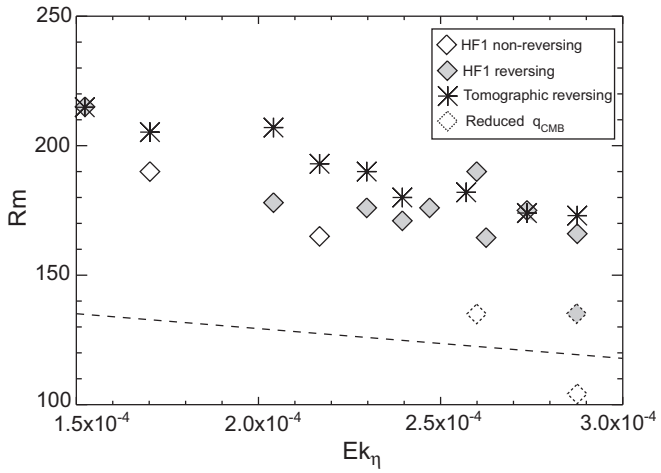

Fig. 9. Magnetic Reynolds number versus magnetic Ekman number from HF1 and tomographic dynamos. Symbols with dashed lines denote reduced CMB heat flow dynamos; unshaded symbols denote non-reversing dynamos. Dashed line is the power law (36), the lower bound of the region of Earth-like dynamo behavior determined by Christensen et al. (2010).

9. Reversal systematics

Systematics of the transition from reversing to non-reversing behavior in these dynamos are shown in Figs. 9 and 10. Fig. 9 shows the portion of the magnetic Ekman number–magnetic Reynolds number plane from Fig. 3 that includes the HF1 and tomographic dynamos. The dashed line is the power law (36) marking the lower bound of the region of Earth-like dynamo behavior determined by Christensen et al. (2010). As anticipated, the transition from non-reversing to reversing behavior in these dynamos lies slightly above (36), although the scatter in Fig. 9 is too large to allow this transition to be defined quantitatively. Nevertheless, the relative positions of our dynamos and the geodynamo to (36) is generally consistent with the interpretation that geodynamo reversals are nearly as sensitive to changes in Rm and Ek_η as our dynamos.

For comparison, Fig. 10 shows the variation in the local Rossby number Ro_l versus age for both the HF1 and tomographic dynamos. Ro_l is a measure of the importance of fluid inertia, and it is known that inertia tends to make dipolar dynamos less stable

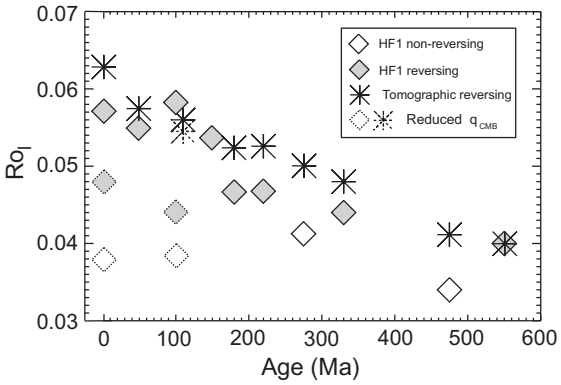

Fig. 10. Local Rossby number versus age from HF1 and tomographic dynamos. Symbols with dashed lines denote reduced CMB heat flow dynamos; unshaded symbols denote non-reversing dynamos.

(Sreenivasan and Jones, 2011). Superimposed on a generally downward trend with age produced by the shrinking inner core and faster rotation, dynamo HF1 has anomalously low values of Ro_l at 275 and 475 Ma. The separation between reversing and non-reversing behavior is slightly clearer in Fig. 10 compared with Fig. 9, however, it is more difficult to extrapolate the trends in Fig. 10 to the core because the length scale of the flow appearing in the definition of Ro_l is poorly constrained.

10. Time average Phanerozoic dynamo structure

Fig. 11 shows CMB heat flux and plate boundary configurations from mantle history HF1 and the corresponding time average dynamo magnetic field on the CMB at ages 100, 180, 275, and 330 Ma. The projections are centered at the latitude and longitude of the reconstruction of Pangaea used by Zhang and Zhong (2011). Growth of the inner core is indicated by the enlargement of the inner core tangent cylinder shown in white.

The CMB heat flux evolves over time from a pattern dominated by spherical harmonic degree 1 during the Paleozoic, associated with the assembly of Pangaea, to a pattern dominated by spherical harmonic degree 2 during the Cenozoic, associated with the breakup of Pangaea, and this transition is reflected in the evolution of the time average magnetic field. As Fig. 11 shows, the time average field at 100 Ma includes magnetic flux concentrations at the longitudes of the two major lower mantle downwellings, and is qualitatively similar in this regard to the structure of the 0–5 Ma time average field shown in Fig. 4. Although the magnetic intensity is low at 100 Ma (because of the high mean CMB heat flux at this time, as discussed earlier) the dipole part of the field is nearly axial, as is the case for the 0–5 Ma paleomagnetic field. With increasing age, the time average field becomes less axially symmetric as the CMB field becomes concentrated in two patches that are offset in longitude. By 330 Ma, the time average north geomagnetic pole of the HF1 dynamo is displaced from the geographic pole in the coordinates of the Pangaea reconstruction. Note the correspondence between the symmetry of the time average magnetic field and the lowest order symmetry of the CMB heat flux heterogeneity, with the magnetic field concentrations aligned with the axis of the high heat flux region on the CMB, and that the field at the CMB retains this basic symmetry until the breakup of Pangaea is well underway.

The reconstructed location of Pangaea is derived from paleomagnetic directions, where it is assumed that the paleomagnetic field has been an axial dipole at all times, the so-called GAD assumption. True polar wander is one well-known factor that complicates the reconstruction of continent locations, particularly during the Mesozoic (Courtillot and Besse, 1987). Our results suggest the possibility that the GAD assumption may also be violated during the time of Pangaea due to the asymmetric the pattern of CMB heat flux at that time.

To test whether the departures from geocentric axial dipole symmetry at the time of Pangaea seen in Fig. 11 are robust, we show in Fig. 12 time averages of the radial magnetic field on the CMB for the HF1 dynamo at 0 Ma and 275 Ma calculated with more realistic parameter values ($Ek = 1 \times 10^{-4}, Ra_\chi = 4 \times 10^6, Pm = 6$, and $Pr = 1$ for the present-day) on a finer grid (1.4° angular resolution and 89 radial levels) using dynamo code MAGIC (Wicht, 2002) averaged over 3 dipole decay times. This parameter combination yields deep-seated dipole-dominant magnetic fields in which most of the dynamo action occurs near the ICB, remote from the CMB heterogeneity. Because of this deep-seated origin, the flux concentrations at the longitudes of the Americas and central Asia are weaker in Fig. 12b than in Fig. 11. Similarly, the 275 Ma dynamo in Fig. 12b is more axial than its higher Ekman number counterpart in Fig. 11, although the primary deviation from axial symmetry, the pair of high intensity magnetic flux patches offset in longitude, is evident in both.

Asymmetry in the pattern of CMB heat flux leads to asymmetric growth of the inner core. Fig. 13 shows the spatial heterogeneity of the time average co-density flux on the ICB at various times according to mantle history HF1. Since the local rate of solidification at the ICB is proportional to the local co-density flux on the ICB, the maps in Fig. 13 indicate how the rate of solidification varies over the ICB since 330 Ma according to mantle history HF1. The polar regions have the slowest growth at all times. Long-lived differences in co-density flux between high and low latitudes imply that the inner core has grown with excess equatorial flattening of the ICB. Relaxation of this excess flattening by solid state creep may contribute to the observed large-scale anisotropy of the inner core through lattice preferred orientation, as advocated by Yoshida et al. (1996). The fastest inner core growth occurs at the longitudes where relatively cold outer core downwellings, initiated at the high heat flux regions on the CMB, reach the ICB. The downwelling produced underneath east Asia is particularly strong at the present-day, and according to HF1, the inner core growth rate is highest there, in agreement with an earlier dynamo model by Aubert et al. (2008) which used a similar pattern of CMB heat flux. It is tempting to speculate that instabilities responsible for the hemispheric dichotomy observed in seismic properties of the inner core, such as the inner core translation (Alboussiere et al., 2010; Monnereau et al., 2010) may be excited by this patch of elevated inner core growth, which in turn is produced by heat flux heterogeneity on the CMB. Note that the northern hemisphere of the inner core shows an overall faster growth rate, a feature that is common to both of our present-day dynamos. At 100 Ma in Fig. 13 the inner core growth is dominantly a spherical harmonic degree and order two pattern of variation at low latitudes, mirroring the pattern of high plate velocity during the opening of the Atlantic. At 180 and 275 Ma, the regions with fastest inner core growth form a tilted pattern aligned with the CMB heat flux pattern.

11. Discussion

Our results indicate that the slow variations in geomagnetic reversal frequency in the Phanerozoic GPTS are more readily explained by core-mantle thermal interaction using a lower mantle history based on time dependent convection, rather than a lower mantle history in which the heterogeneity does not change. Time dependence in mantle convection produces variations in the magnitude and the pattern of heat flux on the CMB that affect dynamo

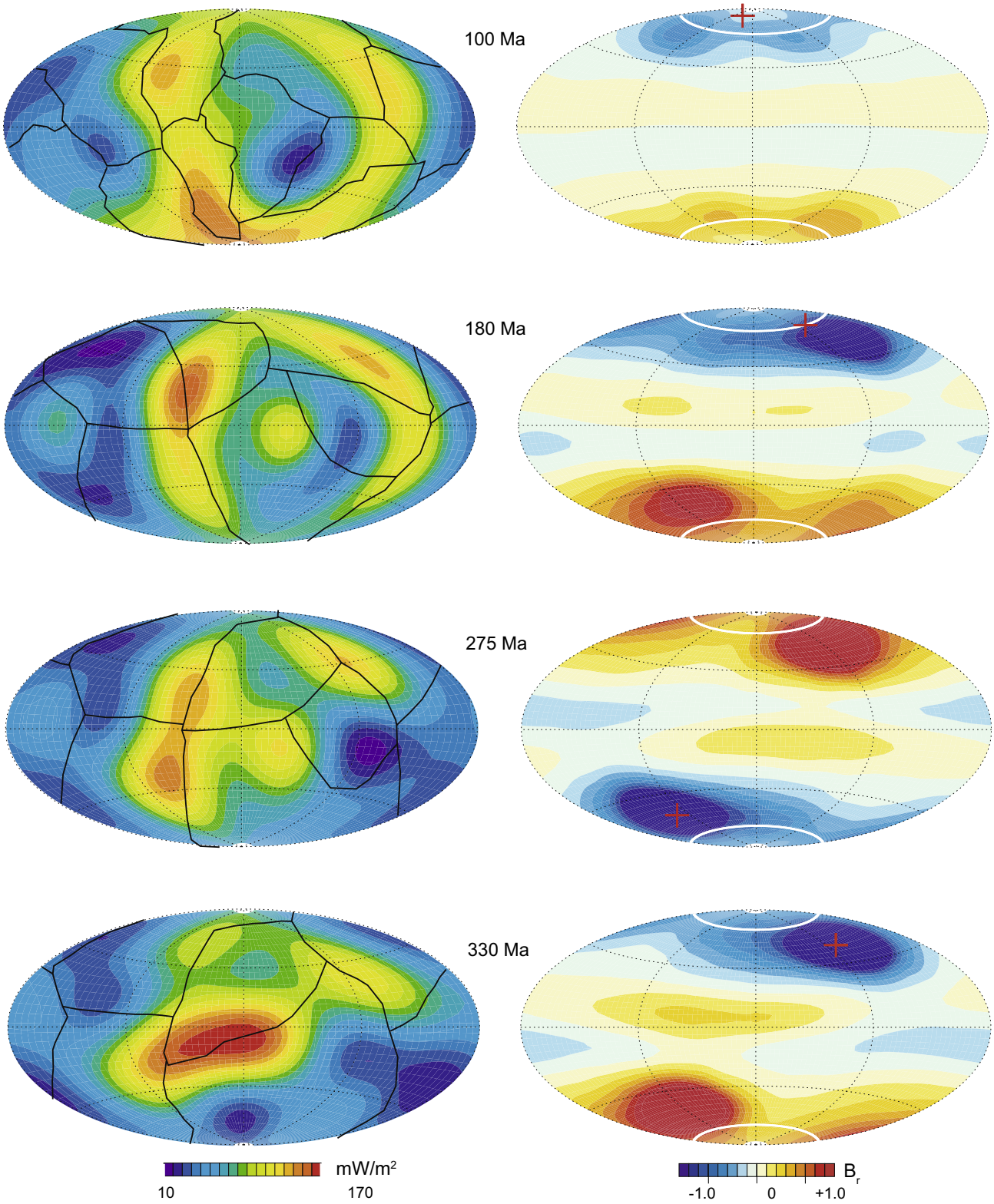

Fig. 11. CMB heat flux and plate boundaries (solid lines) from mantle history HF1 (left) and corresponding time average dynamo radial magnetic field on the CMB (right), at various ages. Magnetic field intensity contours are in dimensionless Elsasser number units, red crosses mark the geomagnetic pole, white curves mark the inner core tangent cylinder. Normal polarity is used for magnetic field averages except at 275 Ma, where reverse polarity is used.

reversal frequency on the time scales comparable to the superchron cycle in the GPTS. Our dynamo driven by CMB heat flux derived from the Zhang and Zhong (2011) mantle history coupled with the observed length of day changes produce reversal cycling, including stable polarity (superchron-like) conditions with large polarity bias around 275 and 475 Ma, respectively, and frequent reversals at other times, reflecting the influence of mantle convection with a supercontinent cycle on the dynamo process. Our numerical dynamo that includes similar length of day changes and total CMB heat flow but assumes a time invariant tomographic

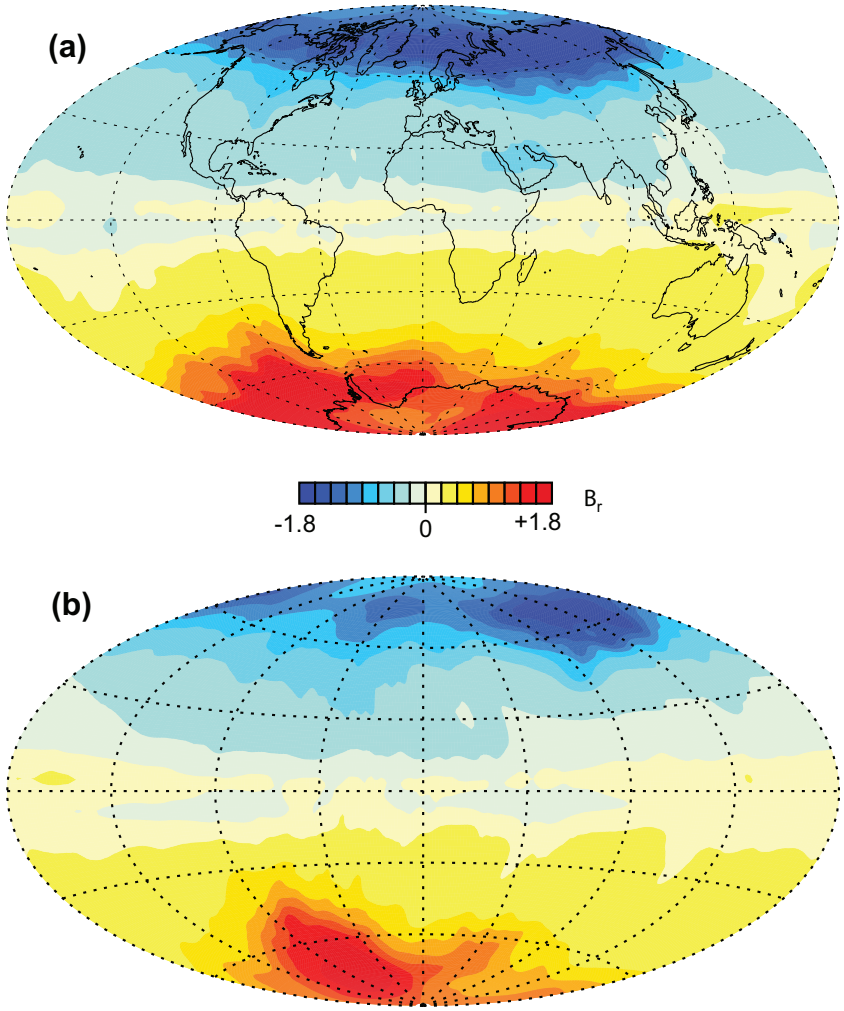

Fig. 12. Time average radial magnetic field on the CMB for (a) 0 Ma and (b) 275 Ma from a high resolution version of dynamo HF1 with parameters given in the text. Magnetic field intensity contours are in dimensionless Elsasser number units.

CMB heat flux heterogeneity yields comparable reversal frequencies prior to Pangaea breakup, but does not yield stable polarity at earlier Phanerozoic times. Both dynamos fail to produce stable polarity conditions around 100 Ma (during the CNS) unless the CMB heat flux is substantially lower than that predicted by either mantle history.

We find that asymmetries in the pattern of CMB heat flux associated with time dependent mantle convection can produce long-lived deviations from geocentric axial dipole field symmetry. In particular, the contribution from spherical harmonic degree 1 heterogeneity to the CMB heat flux associated with supercontinent Pangaea in mantle history HF1 induces magnetic field concentrations on the CMB that are widely separarated in longitude. We also find deviations from uniform growth of the solid inner core. Our dynamos predict that the inner core growth rate is greater in equatorial regions compared to polar regions due to the basic anisotropy of convection in the outer core, and superimposed on this is another pattern of heterogeneous inner core growth that reflects the CMB heat flux heterogeneity at each epoch.

A substantial number of assumptions have been made in order to interface mantle-driven conditions at the CMB to the dynamics of the core, and it is useful to summarize the most important of these, and briefly comment on where improvements can be made in the future. First, our dynamos are driven by two somewhat idealized reconstructions of the Phanerozoic history of the mantle, one assuming time-dependent whole mantle convection, the other assuming the present-day structure of the lower mantle is representative of the deep past. Simple whole mantle convection probably underestimates the true complexity of mantle dynamics, especially in light of the seismic evidence for slab accumulation in the region of the transition zone (Fukao et al., 2001). It is possible, for example, that accumulations of slabs in the transition zone followed by slab avalanche events (Machetel and Thomassot, 2002) could enhance CMB heat flow fluctuations and produce a more variable CMB heat flow history including plume formation events (Larson, 1991), although Zhang and Zhong (2011) found that simply adding the 670 km phase transition does not produce much change in the CMB heat flow in HF1. Reconstructing the CMB heat flow history based on whole mantle convection is highly sensitive to the evolution of plate motions and plate boundaries, both of which become increasingly uncertain with age, so that better-resolved plate motions over a longer period of time are needed for this approach. As for the other approach, the assumption of fixed lower mantle heterogeneity simplifies the history of CMB heat flux by eliminating pattern variability. However, it is not clear that this assumption is dynamically self-consistent. For example, it is difficult to reconcile with the global-scale changes in the structure of mantle flow that seem to be necessary in order to account for the formation and breakup of supercontinents (Phillips and Bunge, 2005; Yoshida and Santosh, 2011), and as our study demonstrates, it is difficult to account for long term reversal cycling.

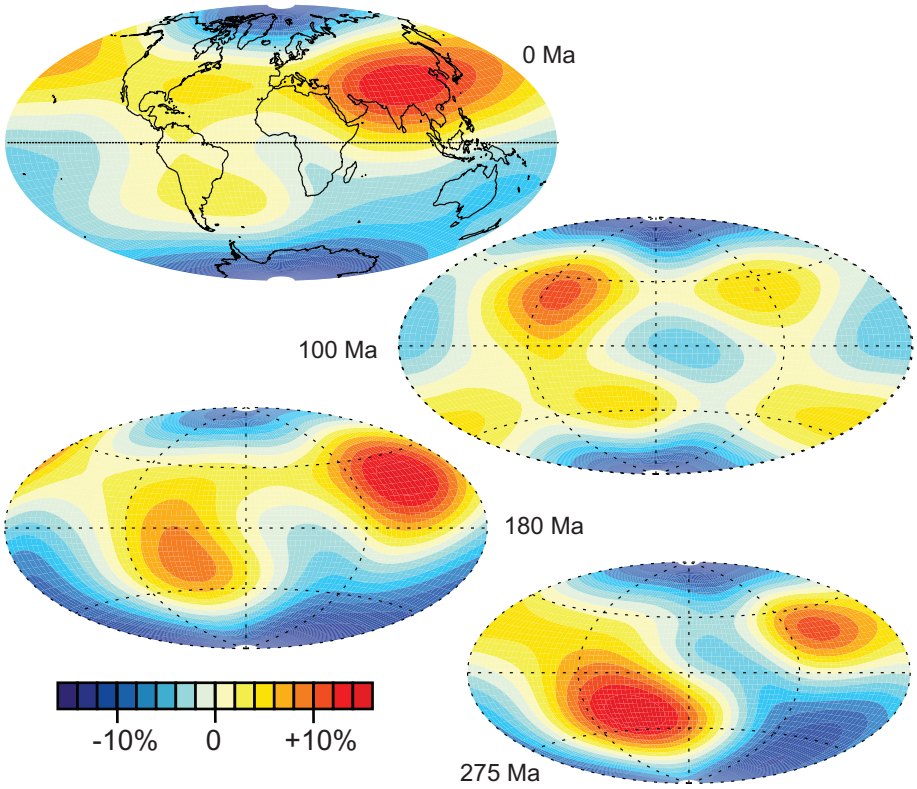

Fig. 13. Variations in the co-density flux on the inner core boundary (representing non-uniform inner core growth rate) at various ages from dynamo HF1. Scale bar denotes percent deviations from the average co-density flux. Image sizes are in proportion to the inner core size at each age, relative to the present-day 0 Ma.

In addition, the dynamo models in this study make numerous simplifications in regard to core dynamics. In particular, they include only the largest scale components of thermal core-mantle interaction, ignore electromagnetic, chemical, gravitational, and topographic interactions with the mantle, and ignore smaller scale thermal perturbations such as plume formation, as well as rotational effects such as true polar wander, tides, and precession. In addition, there are unavoidable problems for numerical dynamos in which computational limitations force key input parameters to have values that are not realistic for the core, or alternatively, are poorly constrained by observations. Parameters that fall into the later category include transport properties such as thermal conductivity, which may be larger in the outer core than we have assumed (de Koker et al., 2012), and also outer core viscosity. We have attempted to circumvent these difficulties by tuning our present-day dynamo input parameters to match the GPTS reversal rate over the past five million years, then extrapolating backward in time along a trajectory in parameter space defined by the thermal evolution of the core using magnetic decay time to calibrate polarity reversal rates. This procedure reduces some of the input dynamo parameter uncertainty, but it has the disadvantage that our results depend very strongly on the dynamo parameters used for the present-day. Lastly, we find that the reversal frequency in our dynamos is sensitive to relatively small changes in the thermal boundary conditions at the CMB, a property that allows us to reproduce some of the extreme variability in GPTS reversal rates through the Phanerozoic with relatively small CMB heat flux variations. Whether this same sensitivity is present in dynamos with more realistic input parameters is a topic ripe for future investigation.

Acknowledgements

This research was supported by Frontiers in Earth System Dynamics Grant EAR-1135382 and Grant EAR-1015669, both from the National Science Foundation. We thank James Ogg for providing the GPTS 2012 polarity time scale in advance of publication, Jean-Pierre Valet for providing the SINT2000 data, and two anonymous reviewers for their helpful comments.

References

Alboussiere, T., Deguen, R., Melzani, M., 2010. Melting-induced stratification above the Earth's inner core due to convective translation. Nature 466, 744–747.
Aubert, J., Amit, H., Hulot, G., Olson, P., 2008. Thermo-chemical wind flows couple Earth's inner core growth to mantle heterogeneity. Nature 454, 758–761.
Aubert, J., Labrosse, S., Poitou, C., 2009. Modeling the paleo-evolution of the geodynamo. Geophys. J. Int. 179, 1414–1428.
Biggin, A.J., Steinberger, B., Aubert, J., Suttie, N., Holme, R., Torsvik, T.H., van der Meer, D.G., van Hinsbergen, D.J.J., 2012. Possible links between long-term geomagnetic variations and whole-mantle convection processes. Nat. Geosci. 5, 526–533.
Buffett, B.A., Huppert, H.E., Lister, J.R., Woods, A.W., 1996. On the thermal evolution of the Earth's core. J. Geophys. Res. 101, 7989–8006.
Burke, K., Steinberger, B., Torsvik, T.H., Smethhurst, M.A., 2008. Plume generation zones at the margins of large low shear velocity provinces on the core-mantle boundary. Earth Planet. Sci. Lett. 265, 49–60.
Burke, K., 2011. Plate tectonics, the wilson cycle, and mantle plumes: geodynamics from the top. Annu. Rev. Earth Planet. Sci. 39, 1–29.
Larson, R.L., 1991. Latest pulse of Earth – evidence for a mid Cretaceous superplume. Geology 19, 547–550.
Christensen, U., Aubert, J., 2006. Scaling properties of convection-driven dynamos in rotating spherical shells and application to planetary magnetic fields. Geophys. J. Int. 166, 97–114.
Christensen, U., Aubert, J., Hulot, G., 2010. How to make an Earth-like dynamo. Earth Planet. Sci. Lett. 296, 487–496.
Cocks, L.R.M., Torsvik, T.H., 2002. Earth geography from 500 to 400 million years ago: a faunal and palaeomagnetic review. J. Geol. Soc. London 159, 631–644.
Cognè, J.P., Humler, E., 2004. Temporal variations of oceanic spreading and crustal production rates during the last 180 My. Earth Planet. Sci. Lett. 227, 427–439.
Courtillot, V., Besse, J., 1987. Magnetic field reversals, polar wander, and core-mantle coupling. Science 237, 1140–1147.
Courtillot, V., Olson, P., 2007. Mantle plumes link magnetic superchrons to Phanerozoic mass depletion events. Earth Planet Sci. Lett. 260, 495–504.
de Koker, N., Steinle-Neumann, G., Vlcek, V., 2012. Electrical resistivity and thermal conductivity of liquid Fe alloys at high P and T, and heat flux in Earth's core. Proc. Nat. Acad. Sci. http://dx.doi.org/10.1073/pnas.1111841109.

Driscoll, P., Olson, P., 2011. Core heat flow driven by superchron cycles. Geophys. Res. Lett. 38, L09304.
Driscoll, P., Olson, P., 2009a. Polarity reversals in geodynamo models with core evolution. Earth Planet. Sci. Lett. 282, 24–33.
Driscoll, P., Olson, P., 2009b. Effects of buoyancy and rotation on the polarity reversal frequency of gravitationally-driven numerical dynamos. Geophys. J. Int. 178, 1337–1350.
Dziewonski, A.M., Lekic, V., Romanowicz, B.A., 2010. Mantle anchor structure: an argument for bottom up tectonics. Earth Planet. Sci. Lett. 299, 69–79.
Dziewonski, A.M., 1984. Mapping the lower mantle: determination of lateral heterogeneity in P velocity up to degree and order 6. J. Geophys. Res. 89, 5929–5952.
Eyles, N., 1993. Earth's glacial record and its tectonic settings. Earth. Sci. Rev. 35, 1–248.
Fukao, Y., Widiyantoro, S., Obayashi, M., 2001. Stagnant slabs in the upper and lower mantle transition region. Rev. Geophys. 39, 291–323.
Gallet, Y., Hulot, G., 1997. Stationary and nonstationary behavior within the geomagnetic polarity time scale. Geophys. Res. Lett. 24, 1875–1878.
Glatzmaier, G.A., Coe, R.S., Hongre, L., Roberts, P.H., 1999. The role of the Earth's mantle in controlling the frequency of geomagnetic reversals. Nature 401, 885–890.
Gubbins, D., Alf'e, D., Masters, G., Price, G.D., Gillan, M., 2004. Gross thermodynamics of two-component core convection. Geophys. J. Int. 157, 1407–1414.
Heller, P.L., Anderson, D.L., Angevine, C.L., 1996. Is the middle Cretaceous pulse of rapid sea-floor spreading real or necessary? Geology 24, 491–494.
Jackson, A., Jonkers, A.R.T., Walker, M.R., 2000. Four centuries of geomagnetic secular variation from historical records. Philos. Trans. R. Astr. Soc. Lond. A358, 957–990.
Johnson, C., Constable, C.G., 1995. The time-averaged geomagnetic field as recorded by lava flows over the last 5 Ma. Geophys. J. Int. 122, 489–519.
Jones, C.A., 2007. Thermal and compositional convection in the core. In: Olson, P., (Ed.), Treatise on Geophysics, vol. 8, Elsevier B.V., pp. 131–186 (Chapter4).
Jones, G.M., 1977. Thermal interaction of the core and the mantle and long-term behavior of the geomagnetic field. J. Geophys. Res. 82, 1703–1709.
Jonkers, A.R.T., 2007. Discrete scale invariance connects geodynamo timescales. Geophys. J. Int. 171, 581–593.
Korte, M., Constable, C.G., Donadini, F., Holme, R., 2011. Reconstructing the Holocene geomagnetic field. Earth Planet. Sci. Lett. 312, 497–505.
Kustowski, B., Ekstrom, G., Dziewonski, A.M., 2008. Anisotropic shear-wave velocity structure of the Earth's mantle: a global model. J. Geophys. Res. 113 (B12), 806306.
Kutzner, C., Christensen, U.R., 2004. Simulated geomagnetic reversals and preferred virtual geomagnetic pole paths. Geophys. J. Int. 157, 1105–1118.
Labrosse, S., 2003. Thermal and magnetic evolution of the Earth's core. Phys. Earth Planet. Inter. 140, 127–143.
Larson, R.L., Olson, P., 1991. Mantle plumes control magnetic reversal frequency. Earth Planet. Sci. Lett. 107, 437–447.
Lay, T., Hernlund, J., Buffett, B.A., 2008. Core-mantle boundary heat flow. Nat. Geosci. 1, 25–32.
Lithgow-Bertelloni, C., Richards, M.A., 1998. Dynamics of Cenozoic and Mesozoic plate motion. Rev. Geophys. 36, 27–78.
Loper, D.E., McCartney, K., 1986. Mantle plumes and the periodicity of magnetic-field reversals. Geophys. Res. Lett. 13, 1525–1528.
Masters, G., Laske, G., Bolton, H., Dziewonski, A.M., 2000. The relative behavior of shear velocity, bulk sound speed, and compressional velocity in the mantle: implications for chemical and thermal structure. In: Karato, S., et al., (Eds.), Earth's Deep Interior: Mineral Physics and Tomography from Atomic to Global Scale, Amer. Geophys. Un., Washington, DC, pp. 66–87.
Machetel, P., Thomassot, E., 2002. Cretaceous length of day perturbation by mantle avalanche. Earth Planet. Sci. Lett. 202, 379–386.
McNamara, A.K., Zhong, S.J., 2005. Thermochemical structures beneath Africa and the Pacific Ocean. Nature 437, 1136–1139.
Miller, K.G., Kominz, M.A., Browning, J.V., Wright, J.D., Mountain, G.S., Katz, M.E., Sugarman, P.J., Cramer, B.S., Christie-Blick, N., Pekar, S.F., 2005. The Phanerozoic record of global sea-level change. Science 310, 1293–1298.
Monnereau, M., Calvet, M., Margerin, L., Souriau, A., 2010. Lopsided growth of Earth's inner core. Science 238, 1014–1017.
Nakagawa, T., Tackley, P.J., 2008. Lateral variations in CMB heat flux and deep mantle seismic velocity caused by a thermal-chemical-phase boundary layer in 3D spherical convection. Earth Planet. Sci. Lett. 271, 348–358.
Nakagawa, T., Tackley, P.J., 2005. Deep mantle heat flow and thermal evolution of the Earth's core in thermochemical multiphase models of mantle convection. Geochem Geophys. Geosyst. 6, Q08003.
Nimmo, F., 2007. Energetics of the Core. In: Schubert, G. (Ed.), Treatise on Geophysics, vol. 8, Elsevier B.V. (Chapter 2).
Ogg, J., 2012. The geomagnetic polarity time scale. in: Gradstein, F., Ogg, J., Schmitz, M., and Ogg, G., (Eds.), The Geologic Time Scale 2012, Eds. Elsevier, Amsterdam, pp. 85–128 (Chapter 5).
Olson, P., Christensen, U.R., 2002. The time-averaged magnetic field in numerical dynamos with non-uniform boundary heat flow. Geophys. J. Int. 151, 809–823.
Olson, P., Driscoll, P., Amit, H., 2009. Dipole collapse and reversal recursors in a numerical dynamo. Phys. Earth Planet. Inter. 173, 121–140.
Olson, P.L., Coe, R.S., Driscoll, P.E., Glatzmaier, G.A., Roberts, P.H., 2010. Geodynamo reversal frequency and heterogeneous core-mantle boundary heat flow. Phys. Earth. Planet. Inter. 180, 66–79.
Pavlov, V., Gallet, Y., 2005. A third superchron during the early Paleozoic. Episodes 28, 78–84.
Petrelis, F., Besse, J., Valet, J.-P., 2011. Plate tectonics may control geomagnetic reversal frequency. Geophys. Res. Lett. 38, L19303.
Phillips, B.R., Bunge, P.H., 2005. Heterogeneity and time dependence in 3 D spherical mantle convection models with continental drift. Earth Planet. Sci. Lett. 233, 121–135.
Poirier, J.-P., Tarantola, A., 1998. A logarithmic equation of state. Phys. Earth Planet. Inter. 109, 1–8.
Ricard, Y., Richards, M.A., Lithgow-Bertelloni, C., Lestunff, Y., 1993. A geodynamic model of mantle mass heterogeneities. J. Geophys. Res. 98, 21895–21909.
Rowley, D., 2002. History of plate creation 180 Ma to present. Geol. Soc. Amer. Bull. 114, 927–933.
Ryan, D.A., Sarson, G.R., 2007. Are geomagnetic field reversals controlled by turbulence with the Earth's core? Geophys. Res. Lett. 34, L02307–12.
Scotese, C.R., 2001. Atlas of Earth history, PALEOMAP Progress Rep. 90-0497, Dep. of Geol., Univ. of Tex. at Arlington.
Sonett, C.P., Kvale, E.P., Zakharian, A., Chan, M.A., Demko, T.M., 1996. Late Proterozoic and Paleozoic tides, retreat of the Moon, and rotation of the Earth. Science 273, 100–104.
Sreenivasan, B., Jones, C.A., 2011. Helicity generation and subcritical behaviour in rapidly rotating dynamos. J. Fluid Mech. 688, 5–30.
Torsvik, T.H., Smethhurst, M.A., Burke, K., Steinberger, B., 2006. Large igneous provinces generated from the margins of the large low-velocity provinces in the deep mantle. Geophys. J. Int. 167, 1447–1460.
Torsvik, T.H., Cocks, R.M., 2004. Earth geography from 400 to 250 Ma: a palaeomagnetic, faunal and facies review. J. Geol. Soc. London 161, 555–572.
Trampert, J., Deschamps, F., Resovsky, J., Yuen, D., 2004. Probabilistic tomography maps chemical heterogeneities throughout the lower mantle. Science 306, 853–856.
Valet, J., Meynadier, L., Guyodo, Y., 2005. Geomagnetic field strength and reversal rate over the past 2 million years. Nature 435, 802–805.
Van der Hilst, R., de Hoop, M.V., Wang, P., Shim, S.-H., Ma, P., Tenorio, L., 2007. Seismostratigraphy and thermal structure of Earth's core-mantle boundary region. Science 315, 1379–1381.
Vanyo, J., Awramik, S., 1985. Stromatolites and earth-sun-moon dynamics. Precambrian Res. 29, 121–142.
Wells, J.W., 1963. Coral growth and geochronometry. Nature 197, 948–950.
Wicht, J., 2002. Inner-core conductivity in numerical dynamo simulations. Phys. Earth Planet. Inter. 132, 281–302.
Wicht, J., Stellmach, S., Harder, H., 2009. Numerical models of the geodynamo: from fundamental Cartesian models to 3D simulations of field reversals. In: Glassmeier, K., Soffel, H., Negendank, J. (Eds.), Geomagnetic Field Variations: Space–Time Structure, Processes, and Effects on System Earth. Springer Berlin.
Williams, G.E., 2000. Geological constraints on the Precambrian history of Earth's rotation and the Moon's orbit. Rev. Geophys. 38, 37–59.
Wu, B., Olson, P., Driscoll, P., 2011. A statistical boundary layer model for the mantle D-region. J. Geophys. Res. 116, B12112.
Yoshida, M., Santosh, M., 2011. Supercontinents, mantle dynamics and plate tectonics: A perspective based on conceptual vs. numerical models. Earth Sci. Rev. 105, 1–24.
Yoshida, S.I., Sumita, I., Kumazawa, M., 1996. Growth model of the inner core coupled with the outer core dynamics and the resulting elastic anisotropy. J. Geophys. Res. B 101, 28085–28103.
Zhang, N., Zhong, S.J., 2011. Heat fluxes at the Earth's surface and core-mantle boundary since Pangea formation and their implications for the geomagnetic superchrons. Earth Planet. Sci. Lett. 306, 205–216.
Zhang, N., Zhong, S.J., Leng, W., Li, Z.X., 2010. A model for the evolution of the Earth's mantle structure since the Early Paleozoic. J. Geophys. Res. 115, B06401.
Zhao, Z.Y., Zhou, Y.Q., Ji, G.S., 2007. The periodic growth increments of biological shells and the orbital parameters of earth-moon system. Environ. Geol. 51 (7), 1271–1277.